

# <sup>1</sup> Reconstructing a physiological state space via <sup>2</sup> chronic jugular microdialysis in freely moving mice

<sup>3</sup>

<sup>4</sup> Michele Nardin<sup>1,\*</sup>, Nan Wang<sup>1</sup>, Soad Elziny<sup>1</sup>, Claire Boyer<sup>1</sup>, Vojko Pjanovic<sup>1</sup>, Luisa Schuster<sup>1</sup>, Peter  
<sup>5</sup> Boklund<sup>2</sup>, Sarah Lindo<sup>1</sup>, Kendra Morris<sup>1</sup>, Anoj Ilanges<sup>1</sup>, Jakob Voigts<sup>1</sup>, Emily Jane Dennis<sup>1,\*</sup>

<sup>6</sup>

<sup>7</sup> <sup>1</sup> Janelia Research Campus, Howard Hughes Medical Institute, Ashburn, VA, USA

<sup>8</sup> <sup>2</sup> CMA Microdialysis AB, Kista, Sweden

<sup>9</sup> \* for correspondence: [nardinm@janelia.hhmi.org](mailto:nardinm@janelia.hhmi.org), [emilyjanedennis@gmail.com](mailto:emilyjanedennis@gmail.com)

## <sup>10</sup> Abstract

<sup>11</sup> Maintaining physiological homeostasis requires a complex interplay among endocrine organs, peripheral  
<sup>12</sup> tissues, and distributed neuroendocrine control circuits, all of which are coupled through feedback loops that  
<sup>13</sup> operate over minutes to hours. Although many physiological needs are broadcast through hormones,  
<sup>14</sup> metabolites, and other chemical compounds circulating in the bloodstream, we rarely observe more than a  
<sup>15</sup> few of these messengers together and at high cadence during behavior. To address this, we developed a  
<sup>16</sup> minimally disruptive workflow to measure the free fraction of hundreds of amines and small peptides at a  
<sup>17</sup> 7.5-minute cadence for ~8 hrs in freely moving mice using chronic jugular microdialysis implants and  
<sup>18</sup> chemical isotope labeling Liquid Chromatography-Mass Spectrometry. Single-compound profiles behave  
<sup>19</sup> according to known physiology, such as purine turnover correlating with movement, delayed  
<sup>20</sup> histamine/5-HIAA changes, and coordinated amino-acid dynamics. Our multiplexed measures enable  
<sup>21</sup> high-dimensional analyses that uncover properties of the underlying dynamics. For example, systems-level  
<sup>22</sup> analyses show that 10 dimensions explain over 70% of the variance in hormone/metabolite covariation,  
<sup>23</sup> consistent with a low rank description of the physiological state space, with projections aligned to locomotion  
<sup>24</sup> state transitions. Our work opens avenues for the discovery of hormonal dynamics, compound interactions,  
<sup>25</sup> and their effects on behavior.

## <sup>26</sup> Introduction

<sup>27</sup> Physiological homeostasis is critical for animal survival. In mammals, bloodborne messengers act as a  
<sup>28</sup> body-wide broadcast medium, traveling through the bloodstream to signal physiological needs to cells  
<sup>29</sup> throughout the body (1–3). Homeostasis is regulated by control circuits in the hypothalamus, brainstem, and  
<sup>30</sup> autonomic ganglia (4–13). For example, orexin cells in the lateral hypothalamus respond to the slope of  
<sup>31</sup> glucose changes rather than its absolute values, and help mediate glucose-dependent decrease in  
<sup>32</sup> locomotion, suggesting that the dynamics of blood chemistry are important signals to the brain and behavior  
<sup>33</sup> (14). Despite the importance of these functions, the study of multiple bloodborne messenger dynamics during  
<sup>34</sup> freely moving, *in vivo* animal studies is still challenging (Supp. Table 1).

<sup>35</sup> Measuring many bloodborne molecules *in vivo* during free behavior presents a technical challenge  
<sup>36</sup> (15). Unlike glucose monitoring, which is performed with simple electrochemical methods, many bloodborne  
<sup>37</sup> molecules, such as amines, peptides, proteins, and steroid hormones, necessitate specialized measurement  
<sup>38</sup> tools and often require blood sampling (16). Restraining animals for repeated collections can increase animal  
<sup>39</sup> stress (17), and whole-blood draws are limited in volume and frequency to prevent hypovolaemia and anemia  
<sup>40</sup> (18–20). Consequently, many studies focus on single analytes or analyze blood only sparsely in time. A

41 minimally disruptive alternative to blood draws is intravascular microdialysis, where a semipermeable  
42 membrane continuously samples the unbound fraction of bloodstream molecules below the molecular weight  
43 cutoff, while leaving platelets and other large molecules in circulation. After calibration, dialysate sample  
44 concentrations can be used to track changes in plasma levels (21–26), resulting in measurements that are not  
45 significantly different from blood draws for several key molecules (27). Clinically, both interstitial and  
46 intravascular microdialysis have already enabled minute-by-minute lactate and glucose monitoring (28) and  
47 steroid hormone profiling over 24hrs periods in humans (29). In rodents, simultaneous blood and brain  
48 microdialysis has been shown to be compatible with behavioral studies (25, 30). However, access to  
49 prolonged-use, easily accessible, and stable jugular microdialysis implants for mice is still challenging.

50 High-frequency blood dialysate samples can be analyzed with modern Liquid Chromatography-Mass  
51 Spectrometry (LC-MS) workflows, such as differential chemical isotope labeling (CIL), to measure hundreds of  
52 bloodborne compounds with high sensitivity (26, 31–33). The multiplexed nature of the measures enables  
53 high-dimensional (high-D) analyses of hormonal data. So far, both experimental and theoretical work have  
54 been constrained to single or low-dimensional (low-D) endocrine control motifs, such as  
55 glucose-insulin-glucagon (34, 35), or HPA cortisol control (36–38). We are inspired by the success of  
56 state-space methods applied to large-scale neural data, gene regulatory networks, and metabolomic profiles,  
57 which have demonstrated that high-D biological data can collapse onto low-D manifolds (32, 39–43). Given  
58 that neural activity, gene regulatory networks, and bloodborne messengers have shared dynamical features,  
59 such as coupled feedback, varying timescales, and coordinated endocrine axes, we wondered if bloodborne  
60 amines and small peptides dynamics also admit a low-rank physiological state space, and whether those  
61 trajectories align with behavioral axes.

62 Here, we introduce a workflow that incorporates chronic jugular microdialysis implants in freely moving  
63 mice, paired with chemical isotope-labeling LC-MS analyses of amine metabolites and small peptides for  
64 state-space reconstruction. We demonstrate the ability to measure hundreds of bloodborne compounds with  
65 stable quality control over nearly 8 hours at a 7.5-minute cadence. This data is compatible with a high-D, low  
66 rank description, with the first 10 principal components explaining more than 70% of the variance.  
67 Furthermore, low-D projections significantly correlate at different delays with locomotion of the animal, opening  
68 the door to systems-level physiology-behavioral studies.

## 69 Results

70 Chronic microdialysis (MD) jugular implants in freely moving mice enable multiplexed,  
71 frequent measurements of plasma compounds

72 Microdialysis (MD) is a technique that uses a semipermeable membrane to collect dialysate samples  
73 from cerebrospinal fluid (CSF), blood, or tissue (44). Most MD applications are acute, or performed within 1-3  
74 days of probe implant (25, 30, 45). Chronic MD probe implants in rats have been used in the brain to monitor  
75 circadian rhythms and in the blood to measure drug concentrations, remaining patent for more than 1 week  
76 and up to 4 weeks (27, 46). In mice, tissue and vascular MD applications have been shown to be feasible in  
77 anesthetized and awake mice (25, 32, 47, 48). However, unlike whole-blood catheters (19), chronic MD jugular  
78 implants that remain patent for at least 7 days and are easily accessible *ad libitum* have, to the best of our  
79 knowledge, not been employed in freely moving animals. This is likely due to classical MD probes using a  
80 bulky liquid cross and stiff materials (Supp. Fig. S1), which make implantation harder than standard jugular  
81 catheters and hinder recovery and movement.

82

83

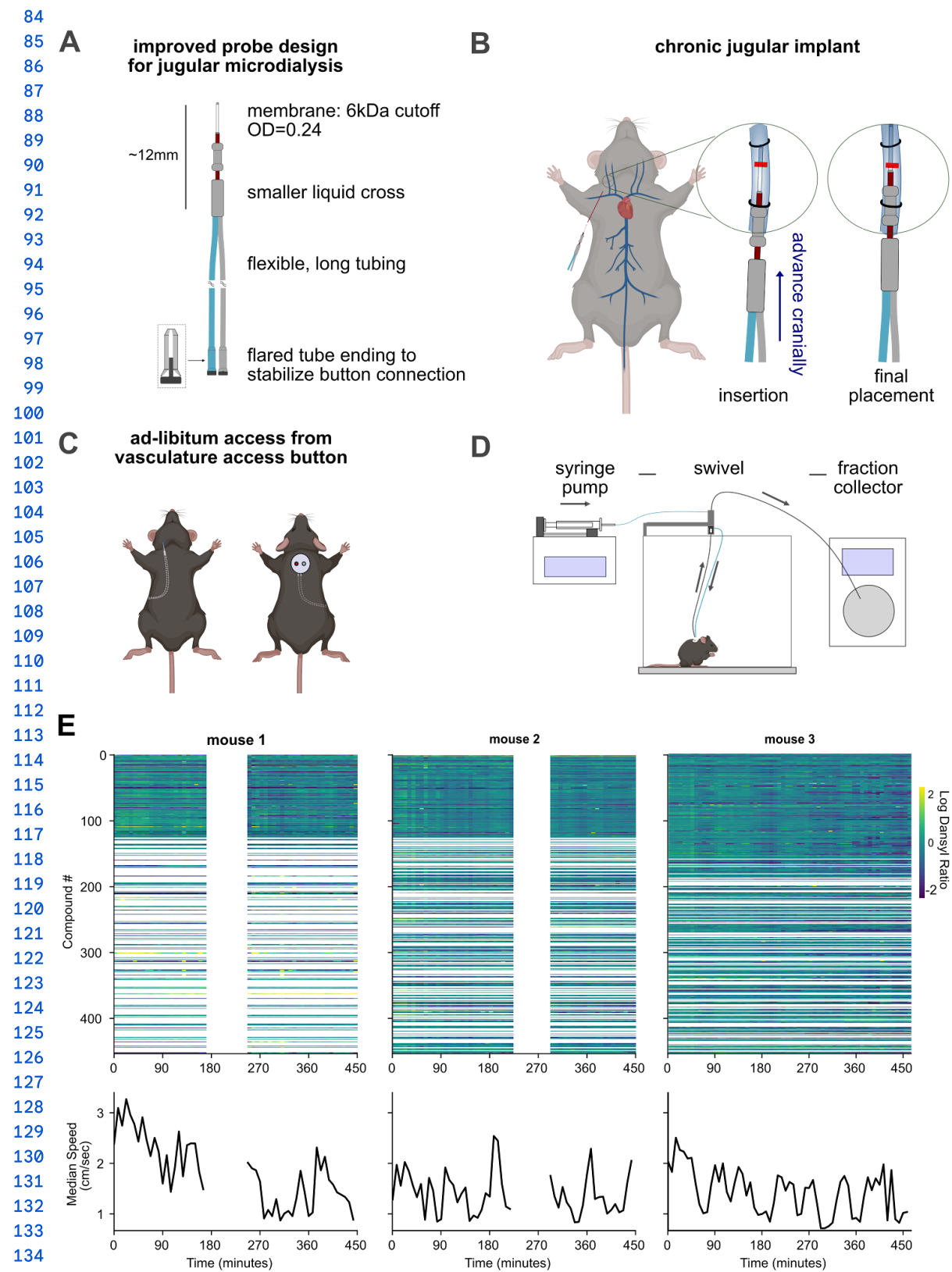


**Figure 1: Chronic jugular microdialysis enables high-frequency, multiplexed blood chemistry in freely moving mice. (A)** Microdialysis (MD) probe with optimized design for chronic jugular implants. Inlet line (blue) and outlet line (gray) connect to the vascular access button (VAB), transition through the redesigned liquid cross, and continue into the probe shaft (red), terminating in a 3.0-mm-long semi-permeable membrane optimized for vascular MD with 6 kDa molecular weight cutoff. **(B)** Surgery cartoon showing the key step for cranial probe advancement and suturing (details in Supp. Fig. S2). **(C)** The flexible tubes loop around the chest with ample space to avoid strain and promote recovery, making the MD implant easily accessible for at least 7 days. **(D)** Experimental flow: syringe pump continuously pumps a saline solution through the jugular MD probe via swivel/tether, which is then collected into a refrigerated fraction collector. Samples are then analyzed offline using differential chemical isotope labeling liquid chromatography-mass spectrometry. **(E)** Representative 6-8 h

141 To overcome this, we designed an optimized probe and a surgery with key enhancements. First, we  
142 employed probes with a smaller liquid cross and suture point, enabling chronic implantation, and  
143 funnel-shaped flared tube endings and soft tubing materials (Fig. 1A). This allows the probe to be implanted  
144 more easily, while also allowing the animal to move more comfortably. The flared tube endings are designed to  
145 be connected to a dual-channel vascular access button (VAB), which is sutured between the scapulae of the  
146 animal. During surgery, the probe membrane is implanted into the jugular and advanced cranially with  
147 standardized placement (Fig. 1B; Supp. Fig. S2). The tubes loop around the chest through a generous tunnel  
148 (Fig. 1C, Supp. Fig. S2). This creates a system that is accessible *ad libitum* by connecting the VAB to a flow  
149 pump and a fraction collector for dialysate samples collection (Fig. 1C-D), and also for delivering perturbations  
150 (21). The full setup consists of an enclosure with a dual-channel swivel that allows the animal to move freely  
151 (Fig. 1D).

152 Using an integrated microdialysis, ultra-high performance liquid chromatography, and mass spec  
153 workflow with differential chemical isotope labeling, we obtained stable, time-resolved profiles of bloodborne  
154 amines, amino acids, small peptides, aromatics, and other molecules (Supp. Fig. S3; Supp. Table 2). In two  
155 animals, a parallel aliquot enabled targeted quantification of steroid hormones, with integrations performed in  
156 Skyline (Methods; data not shown), while we performed untargeted amine metabolomics in all three animals in  
157 IsoMS Pro 1.2.7. Across runs, a background ion at m/z 251.0849 was consistently observed and used to verify  
158 mass accuracy. Its presence and mass, invariant across runs, together with all scan m/z values falling within  
159 expected ranges, indicate stable acquisition and mass accuracy throughout the dataset (Supp. Fig. S3;  
160 Methods).

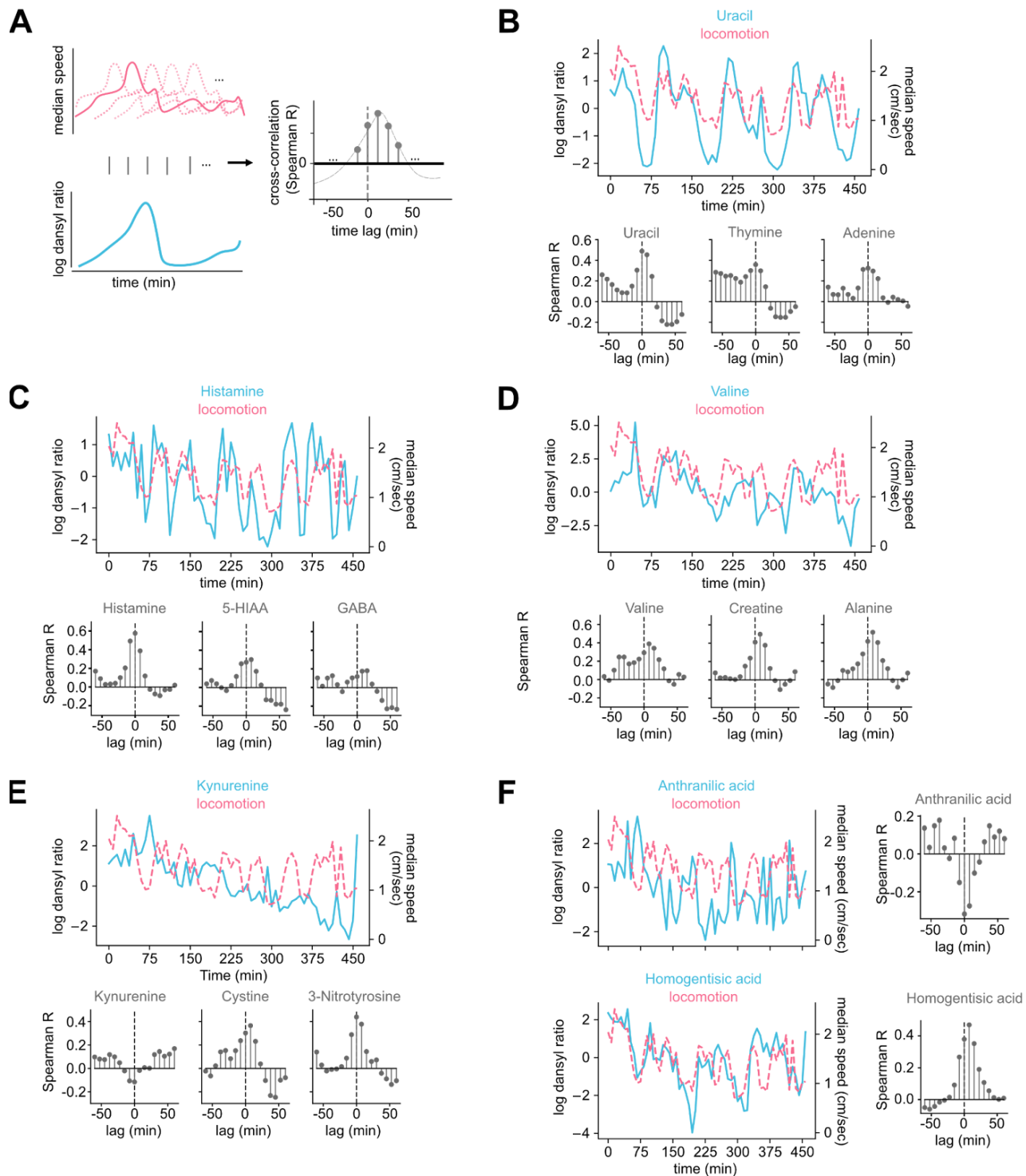
161 Across the 3 animals, we detected 1069, 1471, and 1376 compounds, respectively. Out of those, 241,  
162 343, and 345 passed stringent criteria for RT with an error below 60 seconds (Methods). The intersection  
163 across the three animals, including further restrictions in terms of consistency and replicability across technical  
164 replicates (Supp. Fig. S3), consisted of 123 compounds (Methods). A Bland-Altman plot showed no systematic  
165 bias for high or low chemical isotope labeling ratios (Supp. Fig. S3D).

166 With this setup, we monitored the free fraction of hundreds of amines and small peptides at 7.5-minute  
167 cadence for 6-8 hrs in 3 freely moving mice, together with the speed of the animal, calculated from keypoint  
168 tracking from videos recorded from an overhead camera (Fig. 1E). The implants maintained patency for at  
169 least 7 days post-implant in each animal. In one animal, we performed a control experiment to quantify the  
170 relative recovery of analytes at different flow rates. We found that a flow rate of 1.2  $\mu$ L/min guarantees the  
171 optimal compromise between reliability and temporal precision of the measurement (Supp. Fig. S4). This setup  
172 and data, including a comprehensive metabolomic profiling on microdialyzed rodent blood samples collected in  
173 vivo, allow us to ask how physiological processes relate to behavior.

174 Single-compound analyses recover known relationships between metabolites and  
175 behavior and reveal new ones

176 We measured the dynamics of hundreds of compounds and concomitant locomotion over 6-8 hours in three  
177 mice (Fig. 1E; Supp. Fig. S5). To obtain an overview of the relationship of single compounds and locomotion,  
178 we computed the cross-correlation for all 123 compounds that were validated across all three mice with  
179 locomotion (Supp. Fig. S6). Overall, we found that 87 compounds had significant ( $p < 0.05$ , Bonferroni  
180 corrected) correlation with locomotion, out of which 74 had positive correlation, and 13 negative. Several  
181 relationships suspected in prior work emerged clearly here. To validate this acquisition method as a discovery  
182 tool, we looked specifically at compounds with known relationships between endocrinology, physiology, and  
183 metabolism with behavior (Fig. 2A).

184



185

186 **Figure 2: Single-compound dynamics recapitulate known physiology and reveal new behavior-linked relationships. (A)**  
 187 Cross-correlation workflow: locomotion time series is shifted over lags to quantify delayed alignment (Spearman r). **(B)** Purine turnover  
 188 during movement: Uracil, Thymine, and Adenine correlate with locomotion at 0-7.5-min lag, consistent with exercise-driven pyrimidine  
 189 and purine catabolism. **(C)** Locomotion-related biogenic amines and metabolites: Histamine peaks near zero lag; 5-HIAA (a serotonin  
 190 turnover marker) shows delayed correlation (~7.5 min); GABA exhibits a brief onset-aligned change followed by a reduction. **(D)**  
 191 Amino-acid and energetic pathways: Valine (BCAA), Alanine, and Creatine show positive correlations peaking ~0-15 min after  
 192 locomotion, consistent with nitrogen handling, Cahill cycle, and phosphocreatine replenishment. **(E)** Stress/redox signatures:  
 193 Kynurenone displays negative association with locomotion; Cystine and 3-Nitrotyrosine show positive relationships. **(F)** Additional  
 194 associations not classically linked to locomotion but biologically plausible via pathway context: Anthranilic acid and Homogentisic acid.  
 195 All locomotion/compound time series examples in this figure derived from mouse 3, while cross-correlograms were computed on data  
 196 from the three animals combined.

197 For example, it is well known that muscle contraction and sympathetic arousal ramp up ATP turnover,  
198 leading to an increase of purine and pyrimidine catabolites within minutes (2, 49–51). To that extent, we  
199 measured the Spearman cross-correlation of adenine, uracil, thymine, (Fig. 2B) and xanthine (Supp. Fig. S6)  
200 with locomotion, and found a positive correlation within 0~7.5 minutes lag. This confirms that our approach  
201 captured exercise-induced purine and pyrimidine turnover, which is a known physiological benchmark that, to  
202 our knowledge, had not previously been resolved with this temporal resolution in freely moving mice.

203 Next, we examined compounds related to exercise (Fig. 2C). We analyzed 5-HIAA, which acts as a  
204 readout of serotonin turnover/metabolism (52) and is known to rise after aerobic bouts (53). We also evaluated  
205 histamine, because exercise triggers mast cell histamine formation and post-exercise vasodilation (54, 55).  
206 Finally, we looked at GABA, the chief inhibitory neurotransmitter in the brain (56). We found a high correlation  
207 between microdialysis-measured histamine and locomotion at ~0 lag, and a delayed agreement of 5-HIAA with  
208 locomotion at a lag of 7.5 minutes, as expected from the literature (57, 58). GABA exhibits a weak peak  
209 aligned with the onset of locomotion and a drop after ~22.5 to 45 minutes. The relationships we observe here  
210 highlight the potential of chronic MD to track peripheral correlates of exercise, and could be used as an  
211 exploratory tool to find correlations between states and behavior (59, 60).

212 We next measured the relationship between various amino acids and locomotion (Fig. 2D). Working  
213 muscles exchange amino acids with plasma through the ammonia detox and the glucose-alanine cycle, also  
214 known as the Cahill cycle (49). Branched-chain amino acids are oxidized in increased amounts during exercise  
215 and need to be replenished afterwards (61, 62). Accordingly, we found valine levels to be highest with a 7.5  
216 minute delay compared to locomotion. Alanine is expected to increase with locomotion as part of the  
217 glucose-alanine cycle, where muscle cells release alanine to the liver for gluconeogenesis (63). We found that  
218 alanine was strongly modulated by locomotion at a short delay, in agreement with the literature. Finally, we  
219 analyzed creatine levels compared to locomotion, and found the strongest overall correlation at a delay of 7.5  
220 minutes. This is consistent with creatine's role in replenishing phosphocreatine stores in muscle (64). This  
221 served as an internal validation, showing that these data captured muscle energy flux with the expected delay  
222 kinetics. The ability to track coordinated amino acid and creatine dynamics over minutes provides a resolution  
223 not achievable with previous bulk blood sampling approaches.

224 We also analyzed metabolites in the kynurenine pathway and other markers of locomotion-induced  
225 redox/stress (Fig. 2E). To that extent, we measured the cross-correlation of kynurene, cystine, and  
226 3-nitrotyrosine with locomotion. Kynurene shows a negative correlation with locomotion at zero lag, a result  
227 expected from the literature, as kynurene and its downstream byproducts were found to be altered in older  
228 adults during and after exercise (65). Cysteine shows an interesting trend, with a strong positive correlation at  
229 7.5 minutes lag, and a drop after 22.5 minutes. This might be due to cysteine's roles in multiple pathways,  
230 including protein synthesis, antioxidant activity, and immune function (66). Finally, we analyzed 3-nitrotyrosine  
231 (3-NT), a biomarker of oxidative and nitrosative stress associated with various disease states, aging, and  
232 inflammation (67). We found 3-NT shows a strong positive correlation at no lag with locomotion. These  
233 compound-specific delays and polarity shifts suggest that chronic MD could be used to resolve distinct phases  
234 of oxidative and immune-related metabolism following activity, which is typically collapsed in single-endpoint  
235 blood assays.

236 Further, we found a negative correlation between anthranilic acid and locomotion (Fig. 2F). Anthranilic  
237 acid does not have a direct, established role in mouse locomotion; however, it is a metabolite of the  
238 kynurenine pathway, making the relationship we observed biologically plausible (68, 69). Finally, we also found  
239 an increase of homogentisic acid at 7.5 minutes after locomotion (Fig. 2F). Homogentisic acid is a metabolic  
240 intermediate, normally formed during the catabolism of phenylalanine and tyrosine, and is known for its  
241 involvement in Alkaptonuria, a rare genetic disease which leads to ochronosis, osteoarthritis, and loss of  
242 locomotory capability (70). Although consistent with its role in tyrosine breakdown and dopamine formation,

243 this link to locomotion has not been previously reported. These findings exemplify how high-frequency,  
244 multi-compound monitoring can reveal transient interactions that could be missed in snapshot assays.

245 Finally, we looked for known compound-compound interactions, such as histidine and histamine, which  
246 is produced from histidine (71); arginine and citrulline, which can be produced by nitric oxide synthetase  
247 conversion from arginine (72); and kynurene and N-formylkynurene, which is produced in the same  
248 enzymatic pathway (73) (Supp. Fig. S8). Each pair, as expected, showed a peak correlation at 0 lag.

249 In addition to instantaneous behavioral correlations, we used the binned behavior data and looked for  
250 consecutive collection timepoints where animals had an overall lower or higher median speed. During rest, the  
251 body enters a state of fasting and repair (74). We compared median z-scored compound values during  
252 prolonged immobility vs. persistent locomotion, and found a clear negative correlation, indicating that many  
253 compounds are inversely modulated by locomotion (Supp. Fig. S7). The compound with the largest  
254 locomotion-related change compared to immobility was histamine, which plays a well-known role in  
255 wakefulness (75). Conversely, hydroxycinnamic acid, a microbial metabolite of aromatic amino acids, was  
256 most enriched during rest, as expected from literature on aromatic metabolism in humans (76). Together, these  
257 state-dependent shifts demonstrate that chronic MD can capture systemic biochemical signatures of sustained  
258 activity, which could be used to complement electrophysiological or imaging-based approaches.

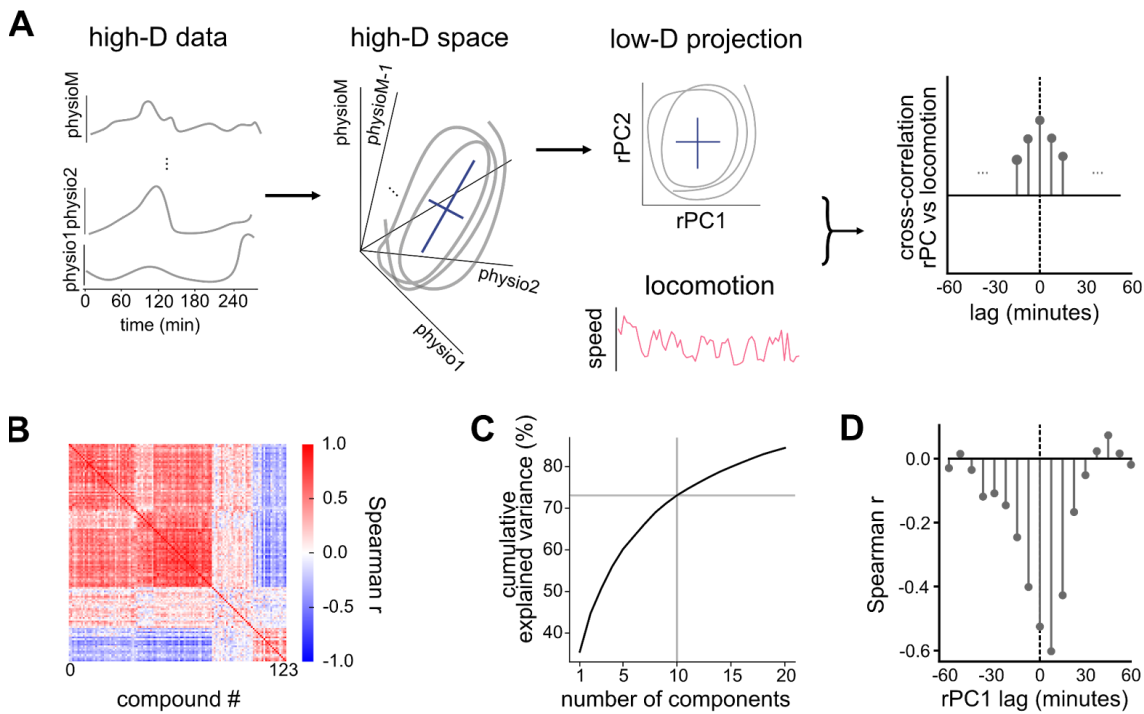
259 Overall, these results demonstrate that chronic MD not only recovers established metabolic signatures  
260 of activity but also uncovers new, biologically plausible relationships that could reveal how behavior  
261 dynamically coordinates metabolism across multiple physiological systems.

## 262 Physiological manifold with behavior alignment

263 Previously, we showed that analyzing single compound dynamics recapitulated known relationships with  
264 locomotion and also uncovered putative novel relationships (Fig. 2, Supp. Fig. S6-S7). Here we take a  
265 systems-level perspective to study the high-D structure of the data and the covariation across compounds (Fig.  
266 3A). We asked whether blood messenger dynamics can be summarized by a small number of latent  
267 dimensions, and whether the projection of the data along these axes aligns with interpretable behavioral  
268 variables. To address this, we employed nonparametric, robust methods to estimate compound covariation  
269 (Spearman's rank correlation) and standard linear decomposition (principal component analysis, PCA) to  
270 extract projections that capture the dominant modes of variance.

271 We begin by considering each compound as a time series: evaluating how it changes over time, and  
272 how it correlates with all other compounds. The resulting matrix exhibited rich structure, with hierarchical  
273 clustering (Ward linkage) ordering compounds into coherent modules (Fig. 3B). As a control, we confirmed that  
274 the Spearman correlation structure was highly similar across the three animals (all cosine similarities > 0.5;  
275 p<1e-10; Supp. Fig. S9A). Because hormonal dynamics may be influenced by locomotion, we also computed  
276 the correlation across compound timeseries discounting the effect of locomotion and observed similarly high  
277 correspondence across datasets (all cosine similarities > 0.5; p<1e-10; Supp. Fig. S9B). Finally, the  
278 Spearman correlation matrices from original and column-normalized data remained highly correlated (all r>0.8,  
279 p<1e-10, Supp. Fig. S9C). Together, these controls confirm that the correlation structure is stable across  
280 animals and robust to technical variation, providing a reliable foundation for analyzing the high-dimensional  
281 organization of physiological dynamics.

282



283

284

285 **Figure 3: A low-dimensional physiological manifold aligns with behavior.** (A) Analysis overview: high-D compound time series →  
286 covariance structure → low-D projections → behavioral alignment tests. (B) Spearman correlation matrix on combined datasets (Ward  
287 linkage ordering) shows prominent block structure (within vs. outside ratio = 4.17) (C) Robust PCA (rank based / Spearman) on the  
288 combined dataset: variance explained vs number of components shows ~73.08% captured by 10 components, rPC1 explains 35.5%.  
289 (D) Cross-correlation between rPCs and locomotion shows rPC1 peaking at 7.5-min lag (gray dashed line marks zero lag). See Supp.  
290 Fig. S10 for Cross-correlations with other rPCs.

291

292 To examine the high-D structure of the data, we computed a Spearman-based, robust PCA, which is  
293 less sensitive to outliers and non-linearity/gaussianity than normal PCA, across the entire dataset of the three  
294 animals combined. We plotted the variance explained by each robust principal component (rPC) (Fig. 3C). We  
295 noticed that the first 10 rPCs explain 73.08% of the variance, with a gentle decay as we add dimensions. In  
296 particular, we notice that the first rPC explains 35.5% of the variance, and the successive rPCs contribute  
297 5~10% each. This indicates that the complexity of circulating molecular dynamics can be represented by a  
298 compact, low-dimensional manifold. This result is reminiscent of NMR-based single snapshot metabolomics  
299 across humans (41), but to our knowledge, it was not previously demonstrated for *in vivo, dynamic*  
300 metabolic profiles recorded in freely moving animals.

301 Next, we examined whether projections along these rPC axes were aligned with locomotion.  
302 Cross-correlation analyses between each rPC and locomotion (Supp. Fig. S10) revealed that rPC1 was  
303 strongly correlated with movement (Fig. 3D, Spearman  $r=-0.59$ ,  $p<1e-19$ ), peaking at a 7.5 min lag. This  
304 suggests that rPC1 represents a coordinated physiological mode driven by locomotor activity. Inspection of  
305 rPC1 loadings showed the highest weights include many amino acids and small peptides: threonine, proline,  
306 alanine, glutamyl-methionine, serine, asparagine, glutamyl-alanine, and histidine. These are muscle- and  
307 nitrogen-related metabolites, and together this indicates the potential ability of our analyses to recover  
308 coherent groups of compounds whose collective dynamics track behaviorally relevant physiological processes.

309 In conclusion, these findings reveal a low-dimensional physiological manifold in which behaviorally  
310 relevant factors, such as those linked to energy and amino-acid metabolism, emerge as dominant axes of  
311 variance. By bridging the single-compound and systems levels views, this approach helps uncover metabolic  
312 coordination with behavior that could not be inferred from traditional single-compound assays. The alignment

313 between global physiological structure and behavioral dynamics highlights chronic microdialysis as a  
314 promising tool for discovering organizing principles of systemic and homeostatic regulation.

## 315 Discussion

316 We present an experimental workflow that lays the foundation for reconstructing a latent, low-rank  
317 physiological manifold from high-frequency measurements of circulating molecules in freely moving mice. By  
318 combining chronic jugular microdialysis (MD) with chemical isotope labeling LC-MS, we track hundreds of  
319 amines and small peptides at 7.5-min resolution over hours (Fig. 1). Single compound dynamics recover  
320 known physiological relationships, such as purine turnover, locomotion-related biogenic amines, and amino  
321 acid metabolism (Fig. 2). Dimensionality reduction methods reveal a compact manifold whose trajectories align  
322 with behavior, such as locomotion (Fig. 3). Together, these results establish technical feasibility, biological  
323 validity, and a systems level description that shifts the focus from single, isolated hormones to coordinated  
324 trajectories in a latent physiological space.

### 325 Why microdialysis and mass spectrometry?

326 Systems and behavioral neuroscience studies could benefit from interdisciplinary methods to study the  
327 drivers of behavior (77). This includes studying how physiological needs are transmitted to tissues and the  
328 brain, and how they influence behavior (78). Many existing readouts in metabolism and endocrinology studies  
329 are downstream byproducts, such as sweat (15, 79), urine (80), and feces (81, 82). These products integrate  
330 multiple upstream processes and can be delayed or confounded by local tissue kinetics; for example, fecal  
331 stress markers are delayed on average by 4~12 hrs compared to plasma levels (83–85). Intravascular MD  
332 directly samples the bloodstream, capturing the unbound fraction of circulating messengers within the probe's  
333 molecular-weight cutoff (21, 25), enabling continuous collection without repeated animal handling stress, and  
334 captures minute-scale dynamics (26). Moreover, given that there is no net fluid exchange, MD is compatible  
335 with hours-long, high-frequency sampling (21, 44). The most similar application is jugular catheter implant for  
336 blood draws in freely moving mice (19). Although this method permits fewer daily samples than microdialysis, it  
337 offers the advantage of providing a comprehensive measure of bound and unbound compound concentrations,  
338 as well as large-scale components, such as platelets and proteins (86).

339 Compared to enzymatic/electrochemical sensors, such as continuous glucose monitors, MD trades  
340 bandwidth (sub-minute intervals) for breadth (hundreds of analytes). With LC-MS, analysis of dialysate  
341 expands the chemical scope to a broad panel of amines and small peptides (31, 33, 82) with minimal  
342 cross-reactivity or sensor drift, at the cost of lower temporal bandwidth and temporal convolution. Moreover,  
343 LC-MS analyses can flexibly incorporate targeted panels (steroids (87), eicosanoids (88), or large  
344 peptides/proteins (89)) so long as they fall within recovery constraints.

345 Finally, the jugular vein provides a suitable sampling site due to its high flow and robust plasma access.  
346 Most cerebral venous blood drains into the external jugular veins, making it an ideal placement for sampling  
347 blood messengers related to neuroscience. The small membrane and shaft footprint, softer tubing, and  
348 compact liquid switch employed here were essential to making a chronic, behavior-compatible jugular implant  
349 feasible in mice, resolving the contradiction between probe bulk/stiffness and the small vasculature (Supp. Fig.  
350 S1-S2). Together, MD-MS offers a scalable approach to capture systemic dynamics across many biochemical  
351 axes simultaneously.

## 352 Transition from single analyte analyses to a physiological manifold view

353 Our single compound analyses reproduce well-known relationships, such as movement-related purine  
354 turnover (50), histamine and 5-HIAA changes consistent with post-exercise vasodilation (54, 55), serotonin  
355 turnover (90), and amino acid activity related to energy and nitrogen handling (50). However, zooming out and  
356 focusing on a systems-level view, the covariation across hundreds of compounds uncovers interesting facts.  
357 For example, principal component analyses capture a large proportion of variance with few dimensions, with  
358 leading axes aligned with interpretable behavior (e.g., velocity vs. rPC1, Fig. 3D). This observation echoes the  
359 low-rank structure described in neural population activity (39) and gene regulatory networks (40), providing a  
360 reduction in complexity to a handful of latent variables. Low-rank structure identification has been a powerful  
361 tool in neuroscience, uncovering principles of motor control (91) and decision-making (91). These results  
362 suggest that endocrine and metabolic control may operate over a compact set of latent variables, contributing  
363 to a growing body of evidence that demonstrates these systems-level methods can be useful in metabolic  
364 research (32, 41–43).

## 365 Future applications and extensions

366 In addition to sampling analytes, microdialysis also enables the delivery of specific molecules and  
367 pharmaceuticals (21). This paves the way for future open-loop and closed-loop experiments, where targeted  
368 perturbations can be performed at will; for example, when the hormonal manifold position falls within a certain  
369 area of state space or an animal performs a specific behavior, such as eating. Closed-loop perturbations tied  
370 to the real-time readout of hormonal levels (92) could include optogenetic stimulation of various brain regions  
371 (e.g., hypothalamus), pharmacological endocrinology manipulations, or nutrient infusion/delivery. On the  
372 modeling side, computational methods can be used to discover low-rank dynamics from high-dimensional data  
373 (94, 95) and detect endocrine-behavioral interactions over different timescales (93). This workflow can also be  
374 integrated with other physiological measurements, such as muscle EMG, implanted thermal RFID tags, or  
375 neural recordings, thus enabling bidirectional mapping between brain activity, effector systems, and circulating  
376 bloodstream messengers.

## 377 Conclusion

378 Chronic jugular MD in freely moving mice, paired with isotope-informed LC-MS, reveals that complex  
379 physiological dynamics collapse onto a low-dimensional manifold with its main axis aligned with locomotion.  
380 This work provides both a technical foundation for minimally disruptive, high-throughput monitoring and a  
381 conceptual shift toward a dynamical-systems physiology of homeostasis.

## 382 Methods

### 383 Surgery

384 All surgeries were done in accordance with animal protocols 25-0281 and 24-0263 approved by the  
385 Janelia Research Campus's Institutional Animal Care and Use Committee. All measurements were performed  
386 on single-housed C57BL/6CRL mice between the ages of 11-15 weeks and between the weights of 26-35g.  
387 Surgeries used sterilized supplies and aseptic techniques in a dedicated surgery space and a stereoscope.  
388 Mice were anesthetized with 3% Isoflurane to reach a surgical plane as confirmed by toe pinch. Following  
389 induction, the ventral neck (mandible to clavicle) and dorsal thorax (neck to rib cage) were shaved, then  
390 cleansed with 70% ethanol. Animals were transferred to a surgical platform, modified to allow passage of the  
391 vascular access button (VAB) through a central opening. The platform was prepared with a nosecone and a  
392 heat source on a sterile field prepared with Press'N Seal film. Surgeons applied ophthalmic lubricant, provided  
393 Ethiqa XR (3.25mg/kg), and surgical sites were scrubbed sequentially with ethanol and chlorhexidine. Animals  
394 were steriley draped with Press'N Seal film wrapped around the torso to retain body heat and act as a sterile  
395 drape. Surgeons applied marcaine to the incision sites (maximum total dose 7mg/kg). A 6-9mm dorsal incision  
396 was made between the scapulae, and a subcutaneous pocket was blunt-dissected for VAB placement.  
397 Rotating the animal as needed, a channel was created subcutaneously from the dorsal incision to the ventral  
398 neck. In the supine position, a 6-9 mm ventral incision was made lateral to the midline over the right jugular  
399 vein (clavicle to mandibular ramus). The VAB was connected to the microdialysis probe, and tubing was  
400 tunneled subcutaneously from the dorsal incision to the jugular site, keeping the tip of the probe capped. The  
401 dorsal incision was closed around the VAB with vicryl suture using a subcuticular continuous suture pattern.  
402 The VAB was connected to a CMA 4004 Syringe Pump with a T1 isotonic sterile perfusion fluid for peripheral  
403 tissue at 10  $\mu$ L/min for 10 minutes, and then reduced to 0.3  $\mu$ L/min for the remainder of the surgery. The  
404 jugular vein was exposed by blunt dissection. Approximately 5-7 mm of the vein was isolated, and two 6-0 silk  
405 ligatures were passed beneath the vessel; one placed caudally at the widest portion of the vein, and the other  
406 cranially, immediately caudal to a small landmark tributary vein, spaced ~3-4 mm apart. Knots were tied in  
407 each silk suture but kept loose enough as not to occlude the vessel. The probe was fed through the loose  
408 caudal suture exterior to the vein and aligned to be inserted. Hemostats were tightened on the tails of the  
409 suture to partially occlude the vessel and reduce bleeding. A small transverse incision was made in the vein  
410 between the two ligatures, and the probe was gently inserted into the vessel lumen and advanced cranially  
411 past the cranial ligature. The cranial ligature was tightened to secure the probe within the vessel, followed by  
412 the caudal ligature. Proper functioning of the probe tip was confirmed by noting the constant presence of  
413 dialysate in the tube exiting the VAB. The skin incision over the vein was closed with Vicryl suture using a  
414 continuous subcuticular suture pattern. A protective metal cap was placed over the VAB to prevent damage.  
415 Post-operative analgesics (ketoprofen 5mg/kg or meloxicam 2mg/kg) were administered daily per protocol,  
416 and animals were allowed to recover under observation.

### 417 Probe design, membrane cutoff, perfusate, and flow rate

418 Probe design followed a design as in Fig. 1A and Supp. Fig. S1B. The membrane molecular weight  
419 cutoff was 6kDa. We employed CMA probes with a smaller liquid cross and suture point, funnel-shaped flared  
420 tube ending for easy yet stable connections, and softer tubing materials for ease of probe implantation and  
421 animal movement. Microdialysis experiments were conducted 5 to 10 days after implantation of the probe. he  
422 During experimental measurements, probes were connected to a syringe pump, and perfused with saline  
423 solution at a flow rate of 1.2  $\mu$ L/min. Microdialysis samples from the blood were collected every 7.5 min. The

424 collected samples were kept at 6-8°C during the sampling and transferred to -80 °C immediately after the end  
425 of the experiment.

## 426 Experimental equipment and procedures

### 427 Sample collection during behavior

428 Behavioral sampling was conducted in a small, circular arena (20cm diameter) equipped with an  
429 overhead camera (Logitech C920). The microdialysis behavioral setup consisted of:

- 430 - Syringe pump (CMA 4004)  
431 - Dual-channel liquid swivel (Instech 375/D/25) mounted over a CMA mouse cage  
432 - Refrigerated fraction collector (CMA 470)

433 The collection procedure consisted of: 1) Pre-recording (setup and stabilization): load and prime syringe, start  
434 devices, flush the probe, and verify stable flow through the swivel and collection lines; 2) Recording (behavior  
435 + sampling): Tether the animal via the VAB and swivel and record behavior while collecting dialysate into  
436 time-stamped vials; 3) Post-recording shutdown and cleanup.

### 437 Routine probe maintenance (Periodic flushing)

438 To maintain patency and minimize tissue buildup around the vascular access, the microdialysis probe was  
439 flushed once daily. During the first 2-3 postoperative days, depending on the animal's condition, wound  
440 healing, and overall recovery, flushes were performed under general anesthesia to reduce tissue strain  
441 (jugular/muscle/skin). Thereafter, daily flushes were conducted in awake animals.

### 442 Computing transit delay and empirical validation

443 Transit delay refers to the time it takes for the liquid to travel from the tip of the probe, where it begins  
444 to interact with the blood, to the fraction collector. To do that, we need to add: half probe DV + VAB button DV  
445 (one connector) + tube from VAB to swivel + swivel center channel + tube from swivel to fraction collector. For  
446 tubing with an inner diameter (ID) 0.12 mm (radius  $r=0.06$  mm), the segment volume is:  $V = l \times \pi \times 0.06^2$   
447 where  $l$  is the length in mm. In our experiments, we calculated an 18.6  $\mu\text{L}$  dead volume, including the swivel,  
448 VAB, connectors, and probe. This, divided by 1.2  $\mu\text{L}/\text{min}$ , yields approximately a 15-minute delay (two  
449 7.5-minute "time bins"), which needs to be accounted for in the analysis. We measured this also in the lab,  
450 where instead of a probe we connected the swivel with a 25cm tube length (which is similar to the dead  
451 volume of MD probe + VAB), and measured 14min 38sec. This is compatible with our theoretical measure, and  
452 we considered 2 time windows (15 minutes) as the delay.

### 453 Dilysate analyses: dansylation and isotope dilution LC-MS/MS + pooled-quality control 454 and internal standard library

455 We paired the microdialysis sample collection with ultra-high performance liquid chromatography  
456 (UHPLC)-mass spectrometry (nanoLC-MS) and differential chemical isotope labeling workflow specifically  
457 designed to measure bloodborne amines and phenols (Supp. Fig. S3). One aliquot of the dialysates was  
458 subjected to nanoLC-PRM (Parallel Reaction Monitoring) for steroid hormone analysis using an Orbitrap  
459 Ascend Tribrid mass spectrometer equipped with a Vanquish Neo UHPLC. The PRM data were analyzed  
460 using Skyline (V24.1). Global metabolomic analysis was done through Compound Discoverer 3.3. Chemical  
461 isotope labeling was performed on 5  $\mu\text{L}$  of the dialysates at each time interval using the dansyl-labeling Kit  
462 from NOVA MT and then analyzed using a VanquishTM Horizon UHPLC connected with an Orbitrap Fusion

463 Lumos Tribrid mass spectrometer (Thermo Fisher Scientific, Bremen, Germany). M/z 251.0849 was selected  
464 as a background peak to check the mass accuracy for the samples. The accurate mass and isotope pattern of  
465 the peak were consistent during all runs, and all scanned m/z are within the expected tolerance, showing good  
466 stability and mass accuracy for the data acquisition.

#### 467 LCMS data processing and selection of compounds

468 The resulting data was interpreted using software IsoMS Pro 1.2.7 (Nova Medical Testing), to extract  
469 peak pairs and calculate the intensity ratio of each peak pair. For metabolite identification, based on multiple  
470 metabolite identifiers, peak pairs were searched against the chemical isotope labeling labeled metabolite  
471 library and linked identity library.

472 Furthermore, after IsoMS Pro software processing (94), we applied the following steps for data cleaning and  
473 compounds selection:

- 474 1) Selection of high-quality compounds: Based on IsoMS Pro 1.2.7 (Nova Medical Testing) data readout,  
475 we selected compounds with Tier 1 and Tier 2 detection quality (RT error < 60sec and reliable  
476 compound detection).
- 477 2) Fraction outlier detection: remove samples with median ratios too low (below median - 4×MAD)
- 478 3) Technical replicates averaging: in log2 scale, we computed the absolute difference among replicates,  
479 and set to blank if  $|rep1-rep2| > 1$ . We then averaged remaining replicates to produce one value per  
480 timepoint.
- 481 4) Selecting consistent subset across animals: We removed compounds from further consideration if they  
482 were missing more than 25% of the LCMS time points for any individual animal. Intersection set  
483 consists of compounds passing the criteria in all three animals.
- 484 5) Interpolation of missing values: each compound time series was linearly interpolated using  
485 `scipy.interpolate.interp1d`.
- 486 6) Z-scoring for manifold analyses: data of each compound is centered and scaled within each animal  
487 using robust z-score  $[(value-\text{median})/\text{MAD}]$ , and then data was concatenated for pooled analyses.

#### 488 Behavioral data acquisition and processing

489 We acquired videos using OBS Studio and a Logitech C920 webcam, acquiring video at 30Hz and  
490 1280 x 720 resolution. For all mice, neck position was tracked using DeepLabCut 3.0.0rc13 (Mathis et al 2018,  
491 Lauer et al 2022) with ResNet-50 convolutional neural networks (He et al 2016). The position and lighting of  
492 the arena changed sufficiently between animals to require a separate network for accurate position  
493 identification. The first two mice were recorded under identical conditions, and we trained the network with 51  
494 manually labeled frames, and tested on 9 held out frames. On the test set, the model achieved RMSE of 7.56  
495 pixels (0.40 cm; 2.0% of the 20 cm arena diameter), with mAP of 80.85% and mAR of 81.11%. Training  
496 performance (RMSE: 2.23 pixels, mAP: 98.92%, mAR: 99.22%) showed a train/test ratio of 3.4x. This network  
497 was applied to the four consistently recorded videos. The second network was trained on 80 training frames  
498 and tested on 4 test frames. The network achieved a test RMSE of 5.24 pixels (0.28 cm), with mAP of 92.71%  
499 and mAR of 94%.

500 Behavioral videos were analyzed at 30 fps using their respective trained networks. For each video, the  
501 x,y tracking coordinates were converted from pixels to centimeters using video-specific calibration  
502 measurements. A representative frame was obtained from each video, and the circular arena boundary  
503 (known diameter: 20 cm) was traced over the image using Adobe Illustrator's Ellipse tool, and the  
504 pixel-to-centimeter conversion factor was calculated from the measured pixel diameter. Calibration factors  
505 averaged  $0.0530 \pm 0.0006$  cm/pixel (mean  $\pm$  SD) across all videos.

506

507 We first removed outliers. We considered two types of outliers: those that had x,y positions outside of the  
508 arena boundary, and any change in coordinates not biologically reasonable. For example, occasionally a  
509 mouse's reflection placed the animal's x,y position outside of the arena, which would be replaced with NaN  
510 (2,111 of 2.4 million frames). Similarly, any single-frame jump in coordinates 10 times higher than the 99th  
511 percentile of observed speed in that video was replaced with NaN (97.5-142.0 cm/s, 1,079 of 2.4 million  
512 frames). Using these filtered data, we calculated a 5-frame centered rolling median filter was applied to smooth  
513 noisy coordinates and camera sensor jitter. The filter computes the median from available values within each  
514 5-frame window, treating flagged outliers as missing data points that do not influence the smoothed trajectory.  
515 The 5-frame window (0.167 seconds at 30 fps) simultaneously allows for the removal of high-frequency noise  
516 while preserving the mouse's biological movements. We computed the speed of the animal as the Euclidean  
517 distance between consecutive coordinates, divided by the time between frames.

518

## 519 Statistics and Multivariate Data Analyses

520

521 Dialysate values are treated as arbitrary units. All analyses focus on within-analyte dynamics, using  
522 per-animal, per-analyte normalization (robust z-score using median and interquartile range). We do not  
523 interpret absolute extracellular concentrations nor between-analyte amplitude differences. We assume  
524 constant recovery over time for each animal and each given analyte. This implies that the measurements are  
525 scaled by a constant factor, hence Z-scoring per compound removes that scale, leaving dynamical properties,  
526 such as those measured by cross-correlation, unaffected.

### 527 Regression analyses

528 Linear regression was used for exploratory relationships between compound concentrations and  
529 behavioral covariates (e.g., locomotion velocity). Prior to regression, compounds were z-scored within an  
530 animal to remove baseline offsets. When applicable, variables were mean-centered to ensure the  
531 interpretability of intercepts.

### 532 Spearman cross-correlation

533 To assess temporal relationships between compound abundance and locomotion, we computed  
534 Spearman rank cross-correlations between each compound time series and the locomotion trace, using  
535 non-parametric rank correlation to reduce sensitivity to outliers. Cross-correlations were computed over  
536 symmetric time lags (-60 to +60 min) using a sliding-window implementation in `scipy.stats.spearmanr`, and  
537 reported as the maximal absolute correlation coefficient within the lag range. Peaks and their lag positions  
538 were used to infer leading or delayed relationships relative to behavior.

539

### 540 Partial correlations

541 To quantify correlations among compounds independent of locomotor influence, we computed partial  
542 Spearman correlations. For each pair of compounds x, y, and confound variable z (locomotion), the partial  
543 correlation was computed as the residual correlation between the rank-transformed residuals of x and y after  
544 regressing out z.

545

546 Immobility vs locomotion analyses

547 We selected two thresholds: locomotion was defined as  $\text{med} + \text{MAD}/2$  ( $\text{med}$  = median of all animal's  
548 medians,  $\text{MAD}$  = median absolute deviation), and immobility was defined as below  $\text{med} - \text{MAD}/2$  for at least 2  
549 time bins. We then analyzed the average z-scored value of each compound during periods of immobility vs  
550 locomotion.

551

552 Robust PCA

553 We performed dimensionality reduction using a Spearman-based robust PCA to capture low-rank  
554 structure while minimizing influence from outliers and non-Gaussian distributions. Each compound time series  
555 was rank-transformed, concatenated across animals after z-scoring, and decomposed using the robust  
556 covariance estimator implemented in `sklearn.decomposition.PCA` with Huber loss. Components (rPCs) were  
557 ordered by explained variance. For behavioral alignment analyses, each rPC time course was cross-correlated  
558 with locomotion as described above. Absolute loading values were used to identify compound groups  
559 contributing to each latent axis.

560 Code availability

561 Original scripts used to generate all the results in this paper, including preprocessing and  
562 supplementary figures, are available at: [https://github.com/michnard/Microdialysis\\_Paper](https://github.com/michnard/Microdialysis_Paper)  
563 All analyses were performed in Python (v3.9 and 3.14) using numpy, pandas, statsmodels, and scikit-learn  
564 packages, with detailed package and environment specifications present in the file "environment.yml" on the  
565 GitHub page for full reproducibility.

566 Data availability

567 Original LCMS data, as well as preprocessed behavior tracking data, were deposited to FigShare:  
568 <https://doi.org/10.25378/janelia.30556511>

## 569 Authors Contributions

570 MN: Michele Nardin, NW: Nan Wang, SE: Soad Elziny, CB: Claire Boyer, VP: Vojko Pjanovic, LS: Luisa Schuster,

571 PB:Peter Boklund, SL: Sarah Lindo, KM:Kendra Morris, AI:Anoj Ilanges, JV: Jakob Voigts, EJD: Emily Jane Dennis

572

	MN	NW	SE	CB	VP	LS	PB	SL	KM	AI	JV	EJD
Conceptualization												
Methodology												
Software												
Formal analysis												
Investigation												
Resources												
Data Curation												
Writing - Original Draft												
Writing - Review & Editing												
Visualization												
Supervision												
Project administration												
Funding Acquisition												

573

574

## 575 Acknowledgements

576 The authors wish to thank Paul Tillberg, Tosif Ahamed, Virginie Ruetten, Pavlo Bulanchuk, Magdalena

577 Schneider, and Ahmed El Hady for discussions, ideas, and support; Guinevere Bell for discussions about

578 surgery and materials; Anne Kuszpit and the whole surgery team for help with surgeries and brainstorming;

579 Rachel Gattoni for Vivarium support; Henrik Jessen for discussions about probe materials and development;

580 Paul Loughnane for setup guidance and discussions on hardware and consumables; Megan Zipperer for help

581 and suggestions on writing style and readability; Boaz Mohar for suggestions on figure schematics and

582 exposition; Wei Wu for assistance in Mass Spec sample prep and analyses. MN used Grammarly for grammar

583 check and Biorender for schematics. Link to license: <https://BioRender.com/lxgr5j6>

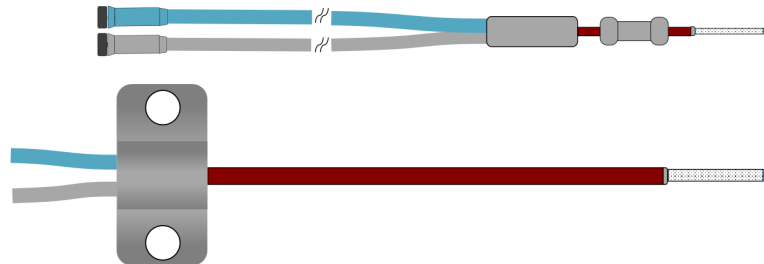
584

## 585 Supplementary Material

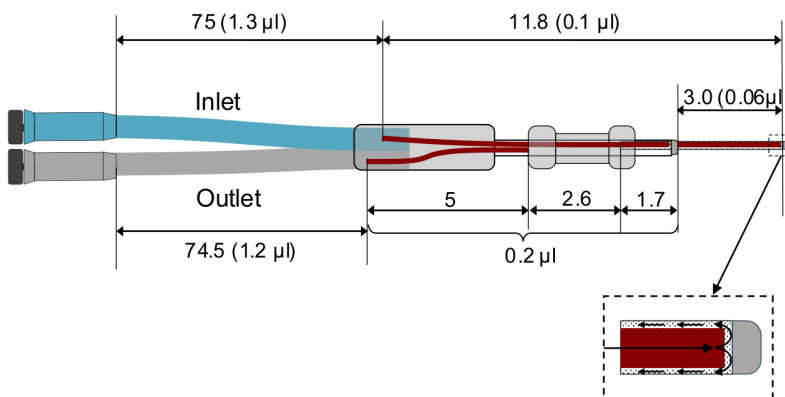
### 586 Supplementary Figures

587

**A**



**B**



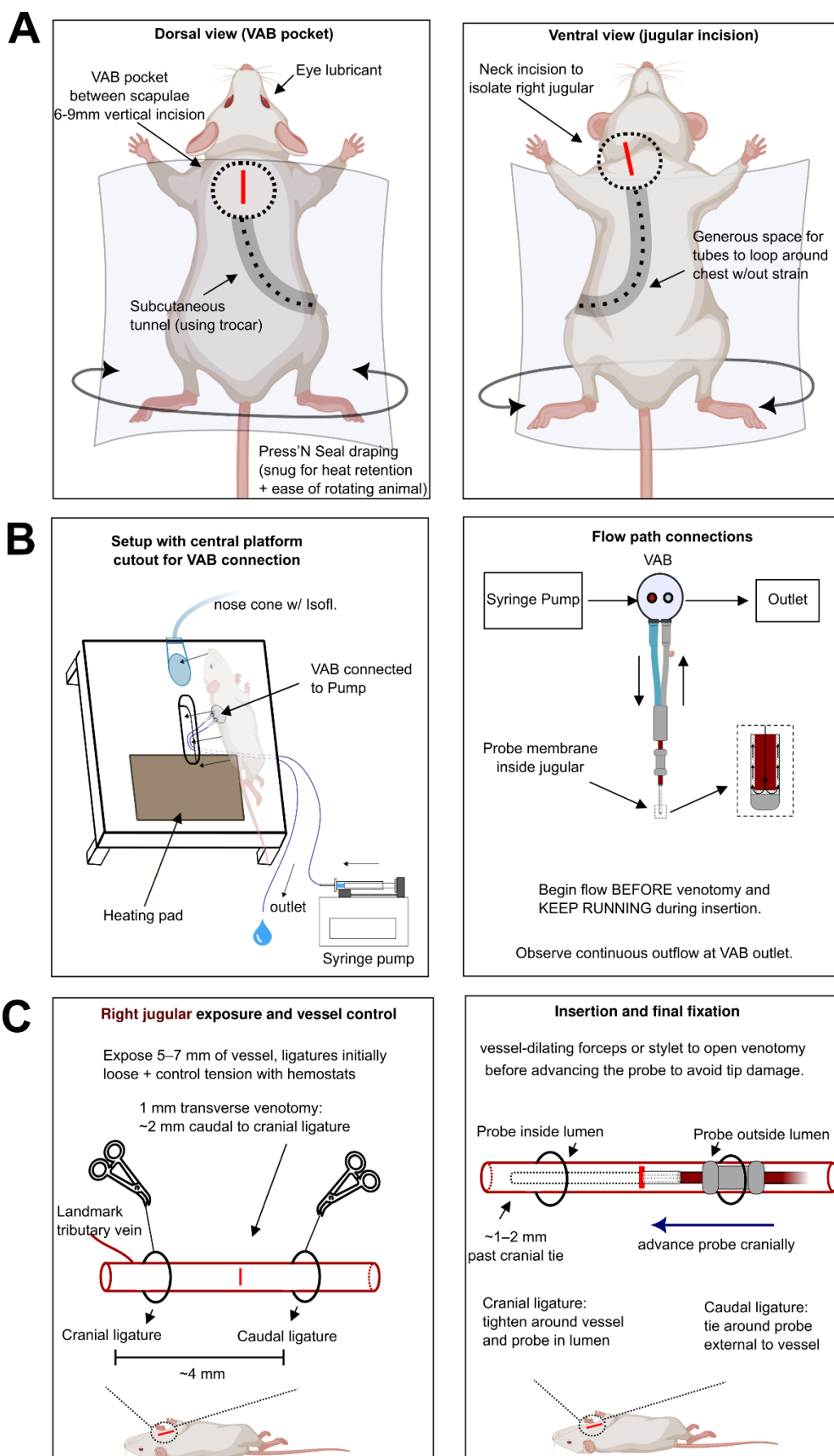
588

#### 589 Supplementary Figure S1: Probe design details.

590 (A) Comparison of our optimized, redesigned MD probe (top) vs standard MD probe for tissue sampling (to  
591 scale). (B) Dimensional schematic and internal volumes: Lengths are in mm, dead volumes ( $\mu\text{l}$ ) are shown in  
592 parentheses. From the Y/connector to the membrane start, the inlet tube is 75 mm ( $\sim 1.3 \mu\text{l}$ ) and the outlet tube  
593 is 74.5 mm ( $\sim 1.2 \mu\text{l}$ ). The connector block contributes 11.8 mm ( $\sim 0.1 \mu\text{l}$ ). The membrane length is 3.0 mm  
594 ( $\sim 0.06 \mu\text{l}$ ). Short shaft segments near the tip are indicated (5, 2.6, and 1.7 mm), with a small pre-membrane  
595 lumen of  $\sim 0.2 \mu\text{l}$ . Inset: tip cross-section illustrating perfusate flow inlet to membrane region.

596

597  
598  
599  
600  
601  
602  
603  
604  
605  
606  
607  
608  
609  
610  
611  
612  
613  
614



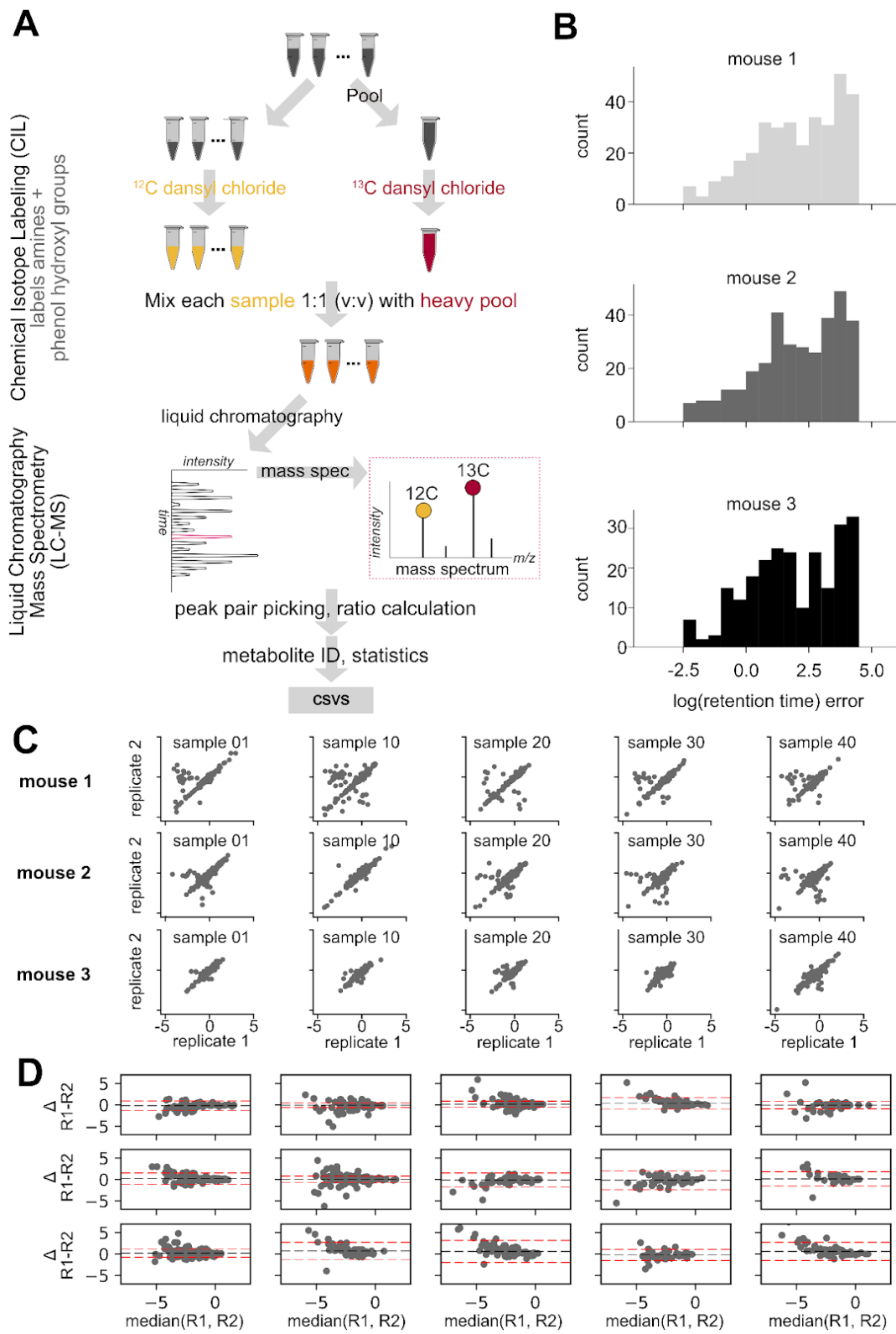
Supplementary Figure S2:  
Vascular-access  
button-assisted jugular  
microdialysis in mouse.

**(A) Left:** Mouse is draped with Press'N Seal (snug to retain heat and allow easy rotation). A 6–9 mm midline dorsal incision is made between the scapulae to form the VAB pocket. A subcutaneous tunnel is created using a trocar from the VAB pocket to the neck. **Right:** On the ventral side, a short neck incision is made to isolate the right jugular vein. Leave generous space for tubing to loop around the chest to provide strain relief.

**(B) Left:** Setup on a heated platform with a central cutout that accommodates the VAB seated subcutaneously between the scapulae; nose cone delivers isoflurane. **Right:** Connect syringe pump → VAB inlet → probe → VAB outlet → collection, and begin flow before the venotomy; observe continuous outflow at the VAB outlet.

**(C) Left:** Expose 5–7 mm of the right jugular. Identify the dorsolateral tributary as the cranial landmark. Place two 6-0 silk ligatures 3–4 mm apart, both initially loose, and apply opposing hemostats for gentle partial occlusion. Plan a 1 mm transverse venotomy ~2–3 mm caudal to the cranial ligature. **Right:** Advance the probe cranially so the tip lies ~1–2 mm past the cranial ligature inside the lumen. Tighten the cranial ligature around the vessel and probe (non-occlusive), then tie the caudal ligature around the probe external to the vessel. Keep flow running and verify continuous outflow.

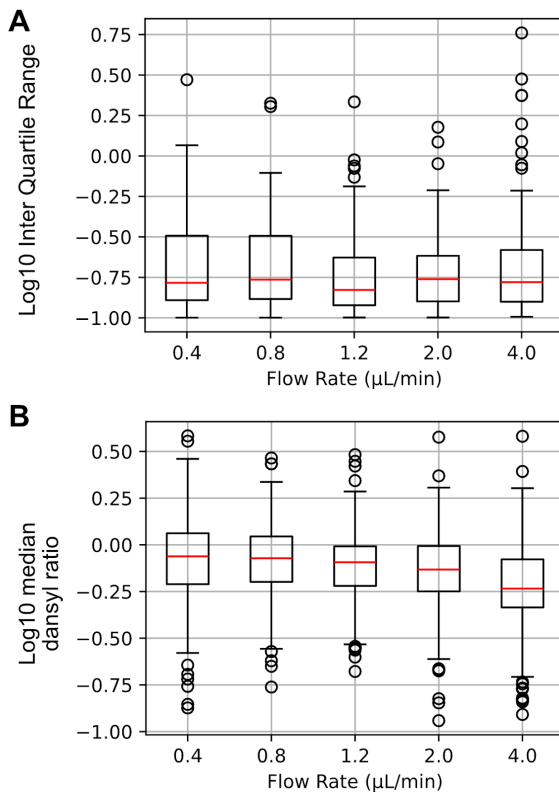
647



648

**649 Supplementary Figure S3: Chemical isotope labeling LC-MS workflow and analytical quality control.** **(A)** Sample  
650 preparation and chemical Isotope labeling LC-MS workflow for amines and small peptides. **(B)** Drift-corrected  
651 retention-time (RT) error distributions per animal. **(C)** Technical replicate scatter plots (log scale). **(D)** Bland-Altman plots  
652 (difference vs. mean replicate); dashed lines represent 95% confidence interval (CI).

653

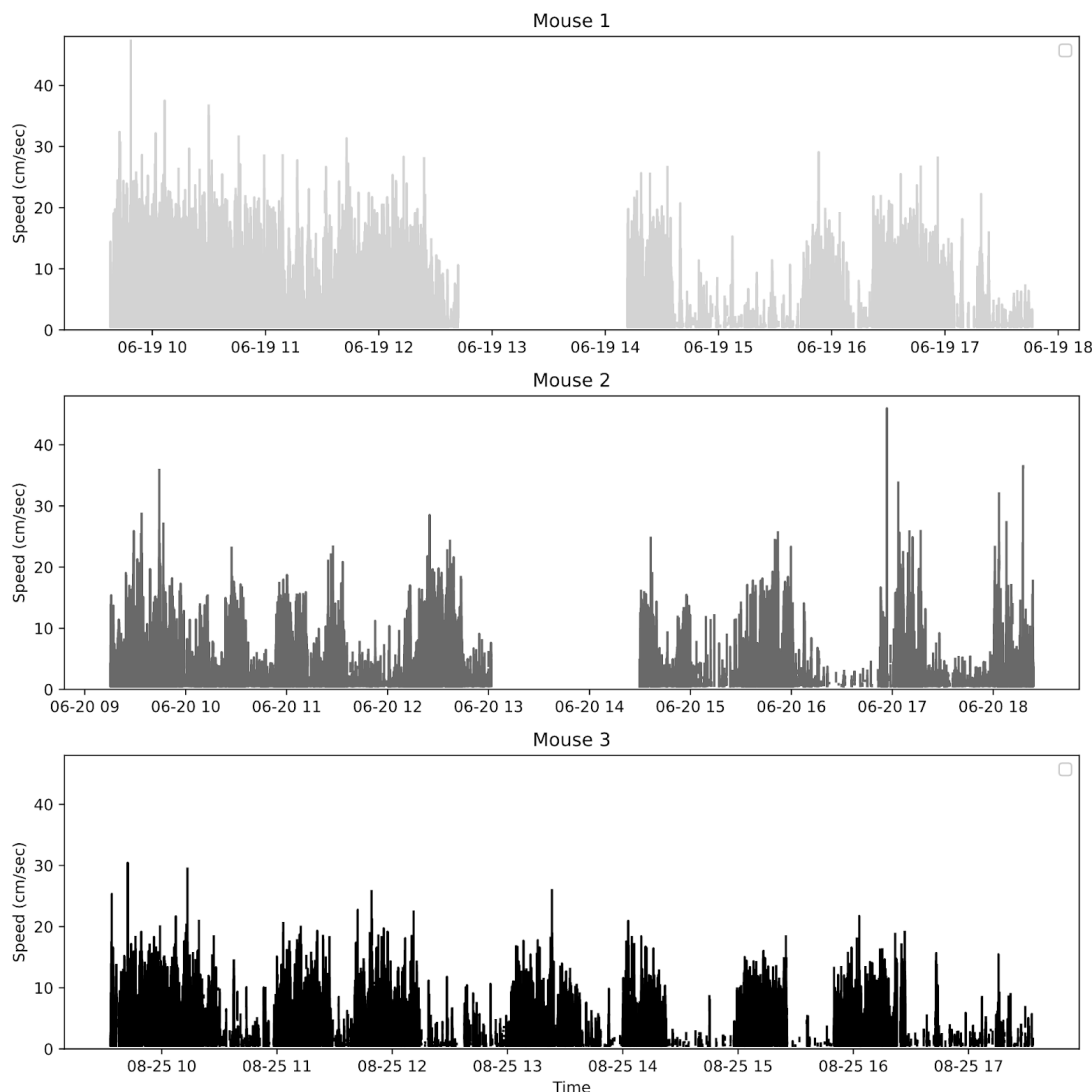


654

655 **Supplementary Figure S4: Relative recovery vs flow rate.**

656 Dialysate signal statistics across flow rates (0.4-4.0 μL/min) to analyze the tradeoff between recovery and temporal  
657 precision. For each flow rate, we collected 20μL samples, which were divided into three subsamples with two technical  
658 replicates each. **(A)** Boxplot for the distribution of interquartile range across 6 technical replicates. Lower is better. **(B)**  
659 Boxplot for the distribution of median dansyl ratio across the 6 replicates. Higher is better.

660



661

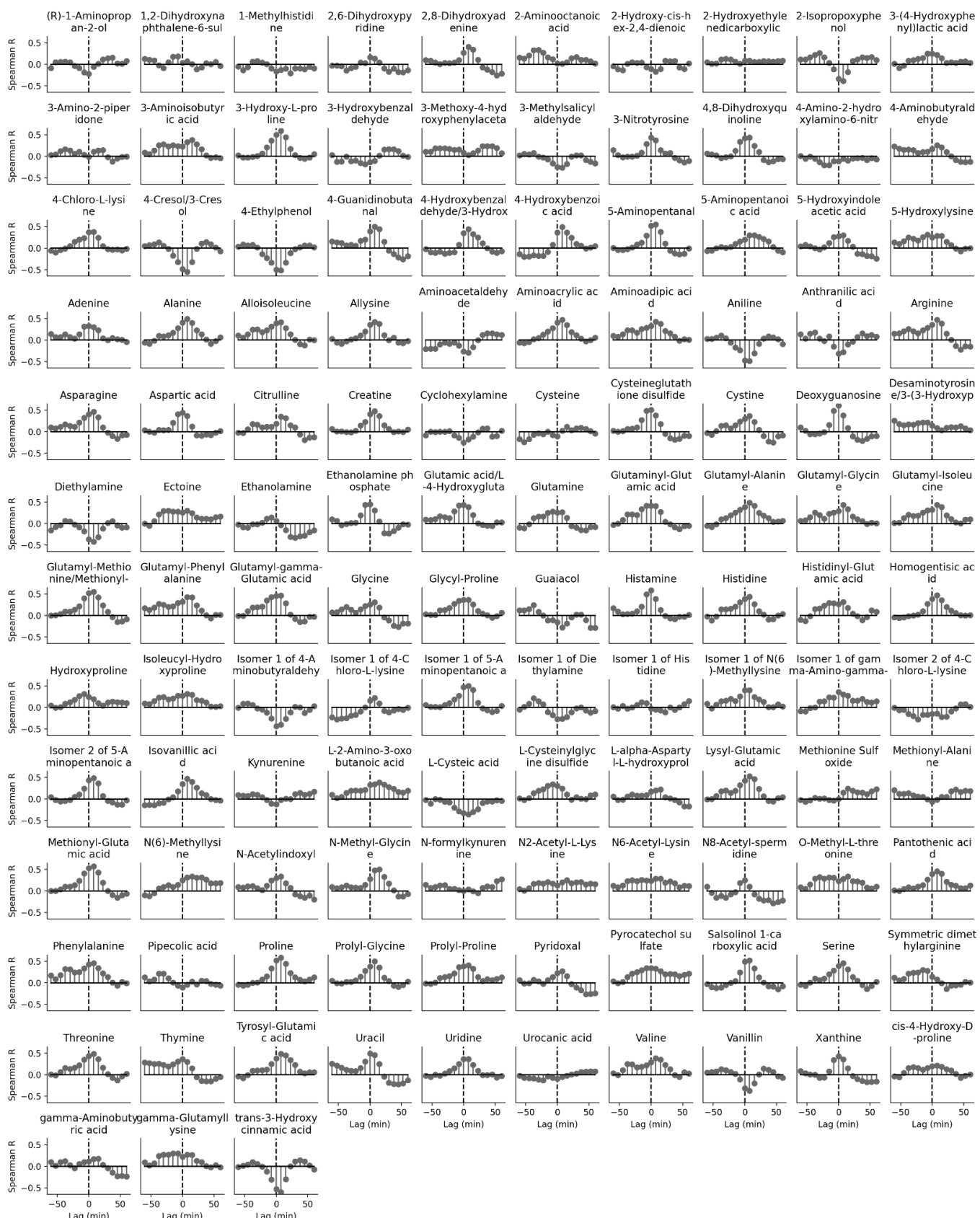
662

663 **Supplementary Figure S5: Mouse locomotion across hours of recordings in three mice during MD recordings.**

664 Speed traces over ~8 h illustrate alternating bouts of movement and immobility that structure our physiology vs. behavior

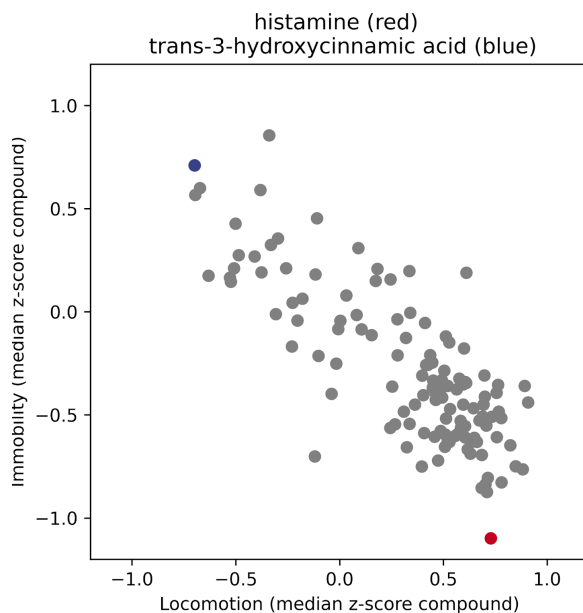
665 analyses.

666



667

668 Supplementary Figure S6: Grid of per-compound cross-correlations with locomotion across lags (-60 to +60 min,  
669 7.5-min steps) for the 123-analyte high-quality intersection across animals.



670

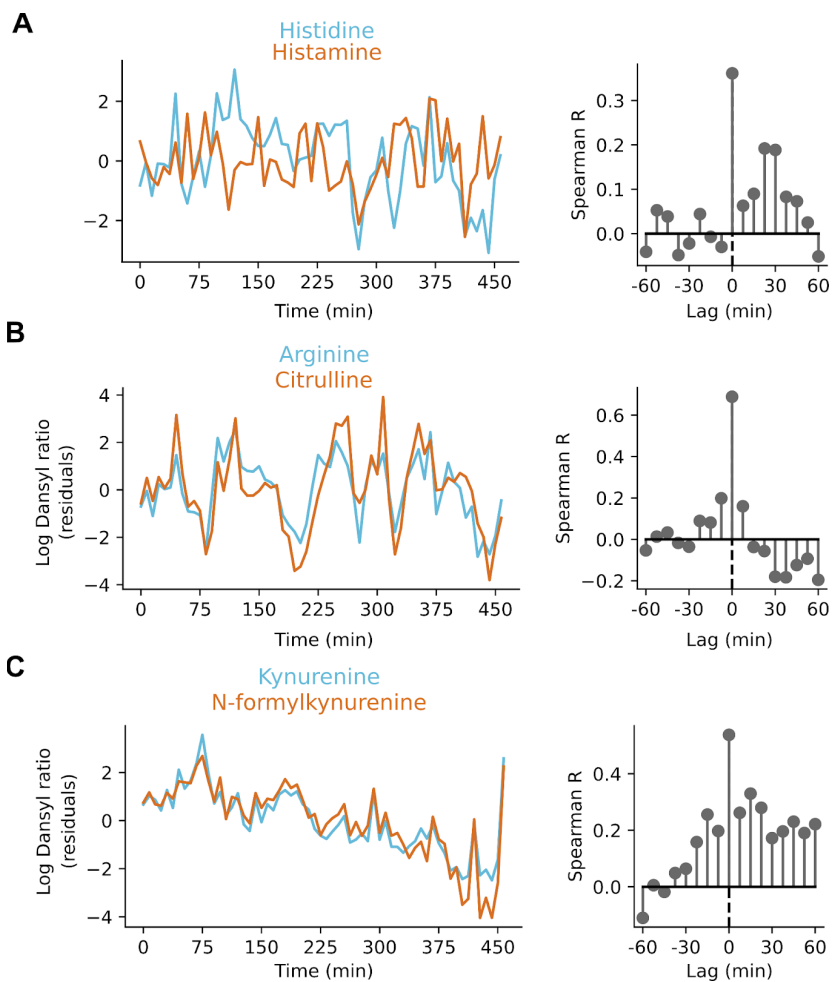
671 **Supplementary Figure S7: Immobility vs locomotion compounds.**

672 We selected two thresholds:  $\text{med} \pm \text{MAD}/2$  ( $\text{med}$  = median,  $\text{MAD}$  = median absolute deviation) of locomotion measured in  
673 7.5 min bins, and define immobility where animal avg. locomotion was below  $\text{med} - \text{MAD}/2$  for at least 2 time bins, and  
674 locomotion when the animal avg. locomotion was above  $\text{med} + \text{MAD}/2$  for at least 2 time bins. Each point in the plot  
675 corresponds to the average z-scored value of each compound during periods of immobility vs locomotion, with red and  
676 blue highlighting Histamine and Hydroxycinnamic acid, respectively.

677

678

679

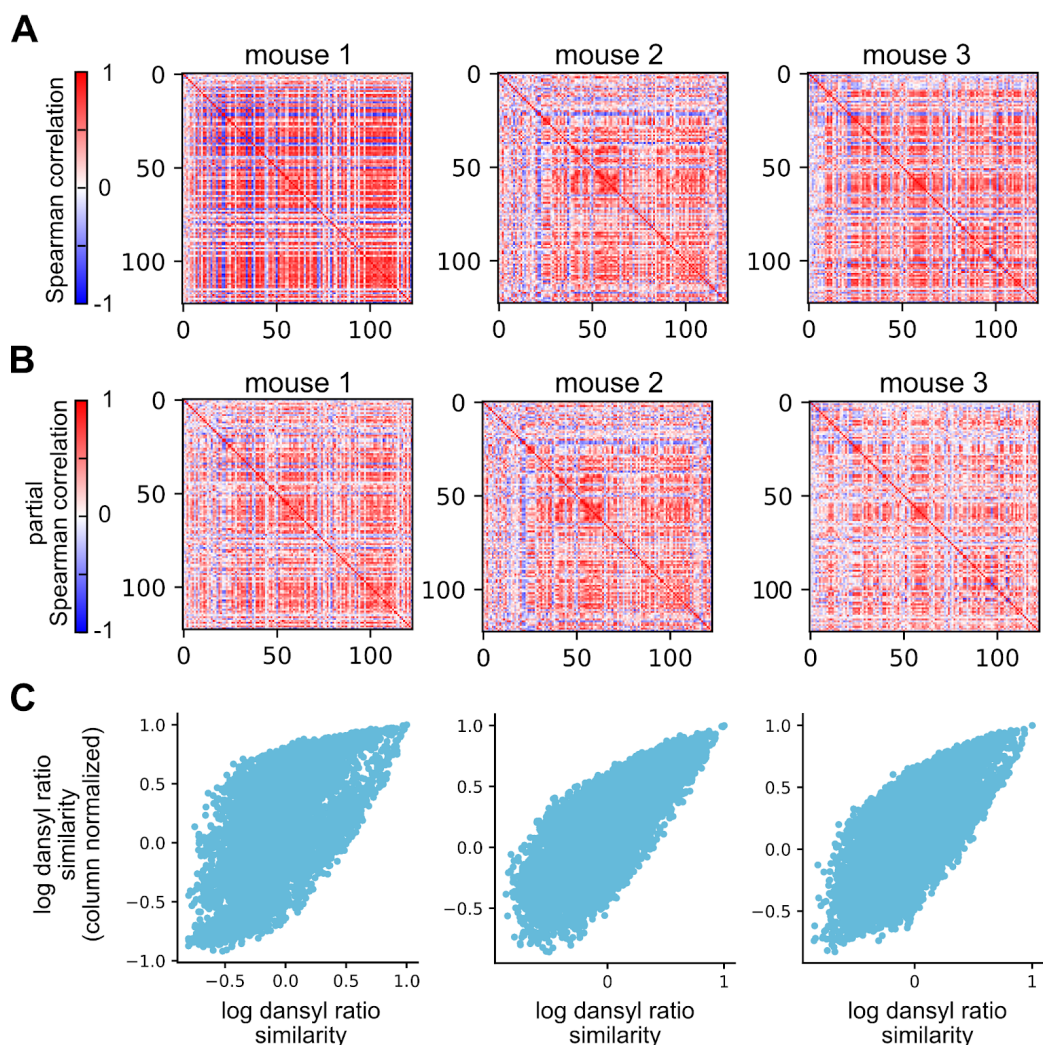


680

681 **Supplementary Figure S8: Interactions across compounds expected from literature.** Analyses of  
682 locomotion-corrected compound timeseries interactions focusing on 3 literature-backed examples using data  
683 only from animal 3. **(A)** Histamine is produced from histidine through decarboxylation (71); **(B)** Nitric oxide  
684 synthase converts arginine to citrulline (72); **(C)** Arylformamidase converts N-formylkynurenone to kynurenone  
685 (73).

686

687



688

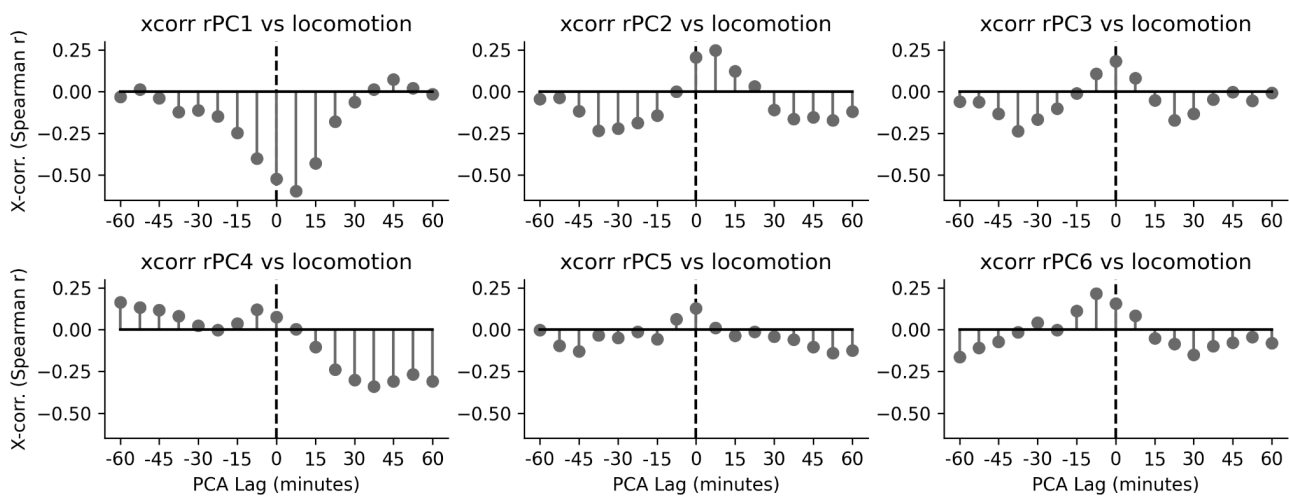
**689 Supplementary Figure S9: Stability of covariation structure across animals and controls.**

**690 (A)** Spearman correlation matrices per animal (Cosine similarity across matrices all > 0.5, p<1e-10). **(B)** Partial  
691 correlations controlling for locomotion (Cosine similarity across matrices all > 0.5, p<1e-10). **(C)** To rule out  
692 potential artifacts from time-varying recovery (e.g., due to blood flow or temperature), we z-scored the  
693 log-ratios of each sample. Sample-wise normalization preserves the correlation structure (each animal's  
694 Spearman's rank correlation coefficient > 0.8, p<1e-10). Scatterplot for the three animals' original vs  
695 z-scored compound similarity is shown.

696

697

698



699

700 **Supplementary Figure S10: Behavior alignment across principal components.**

701 Cross-correlations of PCs with locomotion (-60 to +60 min) show the strongest positive alignment for rPC1  
702 with a 7.5 min positive lag.

703

704 **Supplementary Tables**

705

706

	<u>Blood sampling -- vein pricks</u>	<u>Blood sampling -- vascular catheter</u>	<u>Byproducts and external analyses</u>	<u>Biochemical / electrochemical sensors</u>	<u>Microdialysis</u>
Medium	<i>blood</i>	<i>blood</i>	<i>urine, feces, saliva, sweat, genital swab</i>	<i>CSF, blood</i>	<i>CSF, blood, tissue, plasma</i>
Time Resolution	sec - min	sec - min	min-hrs	ms - s	min
Frequency	hrs <sup>-1</sup> /day <sup>-1</sup>	hrs <sup>-1</sup>	min <sup>-1</sup> /h <sup>-1</sup>	s <sup>-1</sup>	min <sup>-1</sup>
Number of Compounds	1000s	1000s	100s	10s	100s
Key References	(17)	(19)	(15, 83–85, 95)	(15, 96, 97)	(21, 22, 26, 30, 32, 44, 98)

707

708 **Supp. Table 1: Comparison of methods for blood profiling during behavior.**

709 Attributes of invasive sampling, non-invasive byproducts, biochemical/electrochemical sensors, and  
710 microdialysis. Across rows, we focus on the medium sampled; the time resolution of the method used, such as  
711 the delay of the measurement compared to the actual circulating compound; the frequency, as in how often the  
712 sampling can be made; the number of compounds that can be measured/recovered with that technique; and  
713 some key references. Microdialysis offers minute-scale cadence, high multiplexing, and compatibility with  
714 freely moving animals.

715

Benzenoids	4-Ethylphenol, Aniline, 4-Hydroxybenzoic acid, Anthranilic acid, Isovanillic acid, 4-Cresol/3-Cresol, 4-Cresol/3-Cresol, 3-Methoxy-4-hydroxyphenylacetaldehyde, Guaiacol, Vanillin, 2-Isopropoxyphenol, "1,2-Dihydroxynaphthalene-6-sulfonic acid", 4-Amino-2-hydroxylamino-6-nitrotoluene, Homogentisic acid
Lipids and lipid-like molecules	2-Hydroxy-cis-hex-2,4-dienoic acid 2-Hydroxyethylenedicarboxylic acid
Nucleosides, nucleotides, and analogues	Uridine Deoxyguanosine
Organic acids and derivatives	1-Methylhistidine, 2-Aminooctanoic acid, 3-Amino-2-piperidone, 3-Hydroxy-L-proline, 3-Nitrotyrosine, 4-Chloro-L-lysine, 5-Aminopentanoic acid, 5-Hydroxylysine, Alanine, Alloisoleucine, Allysine, Aminoacrylic acid, Amino adipic acid, Arginine, Asparagine, Aspartic acid, cis-4-Hydroxy-D-proline, Citrulline, Creatine, Cysteine, Cysteineglutathione disulfide, Cystine, Ectoine, gamma-Aminobutyric acid, gamma-Glutamyllysine, Glutamic acid/L-4-Hydroxyglutamate semialdehyde, Glutamic acid/L-4-Hydroxyglutamate semialdehyde, Glutamine, Glutaminyl-Glutamic acid, Glutamyl-Alanine, Glutamyl-gamma-Glutamic acid, Glutamyl-Glycine, Glutamyl-Isoleucine, Glutamyl-Methionine/Methionyl-Glutamic acid, Glutamyl-Methionine/Methionyl-Glutamic acid, Glutamyl-Phenylalanine, Glycine, Glycyl-Proline, Histidine, Histidinyl-Glutamic acid, Hydroxyproline, Isoleucyl-Hydroxyproline, Isomer 1 of N(6)-Methyllysine, L-2-Amino-3-oxobutanoic acid, L-alpha-Aspartyl-L-hydroxyproline, L-Cysteic acid, L-Cysteinylglycine disulfide, Lysyl-Glutamic acid, Methionine Sulfoxide, Methionyl-Alanine, N-Methyl-Glycine, N2-Acetyl-L-Lysine, N6-Acetyl-Lysine, O-Methyl-L-threonine, Phenylalanine, Pipecolic acid, Proline, Prolyl-Glycine, Prolyl-Proline, Serine, Symmetric dimethylarginine, Threonine, Tyrosine, Tyrosyl-Glutamic acid, Valine, Pyrocatechol sulfate, N8-Acetyl-spermidine, Ethanolamine phosphate
Organic nitrogen compounds	(R)-1-Aminopropan-2-ol, Aminoacetaldehyde, Diethylamine, Ethanolamine, Histamine, Cyclohexylamine
Organic oxygen compounds	Pantothenic acid, 3-Hydroxybenzaldehyde, 3-Methylsalicylaldehyde, 4-Aminobutyraldehyde, 4-Guanidinobutanal, 4-Hydroxybenzaldehyde/3-Hydroxybenzaldehyde, 5-Aminopentalanal, Kynurenine, N-formylkynurenone
Organoheterocyclic compounds	2,6-Dihydroxypyridine, N-Acetylindoxyl, Urocanic acid, 5-Hydroxyindoleacetic acid, Salsolinol 1-carboxylic acid, 2,8-Dihydroxyadenine, Adenine, Xanthine, Pyridoxal, Thymine, Uracil, 4,8-Dihydroxyquinoline
Phenylpropanoids and polyketides	trans-3-Hydroxycinnamic acid 3-(4-Hydroxyphenyl)lactic acid Desaminotyrosine/3-(3-Hydroxyphenyl)propionic acid

716

717 **Supp. Table 2: High-quality intersection compounds used for manifold analyses.** ChemOnt taxonomy  
718 class (99) determined according to PubChemID and automated chemical classification *ClassyFire* (99)  
719 available at <https://cfb.fiehnlab.ucdavis.edu/>.

720

## 721 References

- 722 1. J. A. Russell, Fifty Years of Advances in Neuroendocrinology. *Brain Neurosci. Adv.* **2**, 2398212818812014  
723 (2018).
- 724 2. M. Wilkinson, R. E. Brown, *An Introduction to Neuroendocrinology*, 2nd ed. (Cambridge University Press,  
725 2015).
- 726 3. J. Schulkin, Neuroendocrine Regulation of Behavior. 1–16 (1998).
- 727 <https://doi.org/10.1017/cbo9780511818738.001>.
- 728 4. J. A. Parker, S. R. Bloom, Hypothalamic neuropeptides and the regulation of appetite. *Neuropharmacology*  
729 **63**, 18–30 (2012).
- 730 5. S. M. Sternson, Hypothalamic Survival Circuits: Blueprints for Purposive Behaviors. *Neuron* **77**, 810–824  
731 (2013).
- 732 6. J. C. Brüning, H. Fenselau, Integrative neurocircuits that control metabolism and food intake. *Science* **381**,  
733 eabl7398 (2023).
- 734 7. M. Lovett-Barron, et al., Multiple convergent hypothalamus–brainstem circuits drive defensive behavior.  
735 *Nat. Neurosci.* **23**, 959–967 (2020).
- 736 8. S. M. Sternson, J. N. Betley, Z. F. H. Cao, Neural circuits and motivational processes for hunger. *Curr. Opin.*  
737 *Neurobiol.* **23**, 353–360 (2013).
- 738 9. I. de A. Salgado, et al., Toggling between food-seeking and self-preservation behaviors via hypothalamic  
739 response networks. *Neuron* **111**, 2899–2917.e6 (2023).
- 740 10. Y. Oka, M. Ye, C. S. Zuker, Thirst driving and suppressing signals encoded by distinct neural populations  
741 in the brain. *Nature* **520**, 349–352 (2015).
- 742 11. R. S. Ahima, D. A. Antwi, Brain Regulation of Appetite and Satiety. *Endocrinol. Metab. Clin. North Am.* **37**,  
743 811–823 (2008).
- 744 12. S. Stagkourakis, et al., Anatomically distributed neural representations of instincts in the hypothalamus.  
745 *bioRxiv* 2023.11.21.568163 (2023). <https://doi.org/10.1101/2023.11.21.568163>.
- 746 13. K. S. Kim, et al., A Normative Framework Dissociates Need and Motivation in Hypothalamic Neurons.  
747 (2023). <https://doi.org/10.1101/2023.10.01.560411>.
- 748 14. P. Viskaitis, et al., Orexin neurons track temporal features of blood glucose in behaving mice. *Nat.*  
749 *Neurosci.* **27**, 1299–1308 (2024).
- 750 15. J. Kim, A. S. Campbell, B. E.-F. de Ávila, J. Wang, Wearable biosensors for healthcare monitoring. *Nat.*  
751 *Biotechnol.* **37**, 389–406 (2019).
- 752 16. X. Shen, et al., Multi-omics microsampling for the profiling of lifestyle-associated changes in health. *Nat.*  
753 *Biomed. Eng.* **8**, 11–29 (2024).
- 754 17. C. Musillo, C. Cerri, M. Boffa, F. Franchi, F. Zoratto, Comparison of corticosterone responses to acute  
755 stress in mice following different serial blood collection methods. *Ann. dell'Ist. Super. di sanità* **61**, 102–108  
756 (2025).
- 757 18. P. C. Gunaratna, P. T. Kissinger, C. B. Kissinger, J. F. Gitzen, An automated blood sampler for  
758 simultaneous sampling of systemic blood and brain microdialysates for drug absorption, distribution,  
759 metabolism, and elimination studies. *J. Pharmacol. Toxicol. Methods* **49**, 57–64 (2004).
- 760 19. A. Y. Park, et al., Blood collection in unstressed, conscious, and freely moving mice through implantation  
761 of catheters in the jugular vein: a new simplified protocol. *Physiol. Rep.* **6**, e13904 (2018).
- 762 20. A. L. Whittaker, T. H. Barker, The Impact of Common Recovery Blood Sampling Methods, in Mice (*Mus*  
763 *Musculus*), on Well-Being and Sample Quality: A Systematic Review. *Animals* **10**, 989 (2020).
- 764 21. R. K. Verbeeck, Blood microdialysis in pharmacokinetic and drug metabolism studies. *Adv. Drug Deliv.*  
765 *Rev.* **45**, 217–228 (2000).

- 766 22. P. A. Evrard, G. Deridder, R. K. Verbeeck, Intravenous Microdialysis in the Mouse and the Rat:  
767 Development and Pharmacokinetic Application of a New Probe. *Pharm. Res.* **13**, 12–17 (1996).
- 768 23. F. Schierenbeck, M. W. N. Nijsten, A. Franco-Cereceda, J. Liska, Introducing intravascular microdialysis  
769 for continuous lactate monitoring in patients undergoing cardiac surgery: a prospective observational study.  
770 *Crit. Care* **18**, R56 (2014).
- 771 24. H. M. Shackman, M. Shou, N. A. Cellar, C. J. Watson, R. T. Kennedy, Microdialysis coupled on-line to  
772 capillary liquid chromatography with tandem mass spectrometry for monitoring acetylcholine in vivo. *J.*  
773 *Neurosci. Methods* **159**, 86–92 (2007).
- 774 25. T. Umezawa, T. Sano, J. Hayashi, Y. Shibata, Simultaneous blood and brain microdialysis in a free-moving  
775 mouse to test blood-brain barrier permeability of chemicals. *Toxicol. Rep.* **7**, 1542–1550 (2020).
- 776 26. K. N. Schultz, R. T. Kennedy, Time-Resolved Microdialysis for In Vivo Neurochemical Measurements and  
777 Other Applications. *Annu. Rev. Anal. Chem.* **1**, 627–661 (2008).
- 778 27. H. Yang, Q. Wang, W. F. Elmquist, The Design and Validation of a Novel Intravenous Microdialysis Probe:  
779 Application to Fluconazole Pharmacokinetics in the Freely-Moving Rat Model. *Pharm. Res.* **14**, 1455–1460  
780 (1997).
- 781 28. C. Blixt, O. Rooyackers, B. Isaksson, J. Werner, Continuous on-line glucose measurement by  
782 microdialysis in a central vein. A pilot study. *Crit. Care* **17**, R87 (2013).
- 783 29. T. J. Upton, et al., High-resolution daily profiles of tissue adrenal steroids by portable automated collection.  
784 *Sci. Transl. Med.* **15**, eadg8464 (2023).
- 785 30. T. Umezawa, Blood-Brain Barrier. 203–228 (2025). [https://doi.org/10.1007/978-1-0716-4474-4\\_11](https://doi.org/10.1007/978-1-0716-4474-4_11).
- 786 31. R. Zhou, L. Li, Mass Spectrometry in *Metabolomics*, Methods and Protocols. *Methods Mol. Biol.* **1198**,  
787 127–136 (2014).
- 788 32. L. Wang, Z. Pi, S. Liu, Z. Liu, F. Song, Targeted metabolome profiling by dual-probe microdialysis  
789 sampling and treatment using Gardenia jasminoides for rats with type 2 diabetes. *Sci. Rep.* **7**, 10105 (2017).
- 790 33. A. L. George, et al., Serum/Plasma Proteomics, Methods and Protocols. *Methods Mol. Biol.* **2628**,  
791 477–488 (2023).
- 792 34. R. N. Bergman, Origins and History of the Minimal Model of Glucose Regulation. *Front. Endocrinol.* **11**,  
793 583016 (2021).
- 794 35. C. Cobelli, et al., The Oral Minimal Model Method. *Diabetes* **63**, 1203–1213 (2014).
- 795 36. O. Karin, et al., A new model for the HPA axis explains dysregulation of stress hormones on the timescale  
796 of weeks. *Mol. Syst. Biol.* **16**, MSB209510 (2020).
- 797 37. S. L. Lightman, M. T. Birnie, B. L. Conway-Campbell, Dynamics of ACTH and Cortisol Secretion and  
798 Implications for Disease. *Endocr. Rev.* **41**, bnaa002 (2020).
- 799 38. V. M. Markovic, Z. Cupic, V. Vukojevic, L. Kolar-Anic, Predictive modeling of the  
800 hypothalamic-pituitary-adrenal (HPA) axis response to acute and chronic stress. *Endocr. J.* **58**, 889 (2011).
- 801 39. J. P. Cunningham, B. M. Yu, Dimensionality reduction for large-scale neural recordings. *Nat. Neurosci.* **17**,  
802 1500–1509 (2014).
- 803 40. W. Pindah, S. Nordin, A. Seman, M. S. M. Said, Review of Dimensionality Reduction Techniques using  
804 Clustering Algorithm in Reconstruction of Gene Regulatory Networks. *2015 Int. Conf. Comput., Commun.,*  
805 *Control Technol. (I4CT)* 172–176 (2015). <https://doi.org/10.1109/i4ct.2015.7219560>.
- 806 41. B. Li, J. Su, R. Lin, S.-T. Yau, Z. Yao, Manifold fitting reveals metabolomic heterogeneity and disease  
807 associations in UK Biobank populations. *Proc. Natl. Acad. Sci.* **122**, e2500001122 (2025).
- 808 42. G. Wang, et al., Spatial quantitative metabolomics enables identification of remote and sustained  
809 ipsilateral cortical metabolic reprogramming after stroke. *Nat. Metab.* **7**, 1791–1800 (2025).
- 810 43. R. van de Wetering, et al., Behavioral metabolomics: how behavioral data can guide metabolomics  
811 research on neuropsychiatric disorders. *Metabolomics* **19**, 69 (2023).
- 812 44. M. I. Davies, J. D. Cooper, S. S. Desmond, C. E. Lunte, S. M. Lunte, Analytical considerations for

- 813 microdialysis sampling. *Adv. Drug Deliv. Rev.* **45**, 169–188 (2000).
- 814 45. W. F. Elmquist, R. J. Sawchuk, Application of Microdialysis in Pharmacokinetic Studies. *Pharm. Res.* **14**,  
815 267–288 (1997).
- 816 46. J. Borjigin, T. Liu, Application of long-term microdialysis in circadian rhythm research. *Pharmacol.*  
817 *Biochem. Behav.* **90**, 148–155 (2008).
- 818 47. P. A. Evrard, C. Ragusi, G. Boschi, R. K. Verbeeck, J.-M. Scherrmann, Simultaneous microdialysis in brain  
819 and blood of the mouse: extracellular and intracellular brain colchicine disposition. *Brain Res.* **786**, 122–127  
820 (1998).
- 821 48. C. K. Thoeringer, et al., The temporal dynamics of intrahippocampal corticosterone in response to  
822 stress-related stimuli with different emotional and physical load: An in vivo microdialysis study in C57BL/6 and  
823 DBA/2 inbred mice. *Psychoneuroendocrinology* **32**, 746–757 (2007).
- 824 49. J. Axsom, et al., Quantification of nutrient fluxes during acute exercise in mice. *Cell Metab.* **36**,  
825 2560–2579.e5 (2024).
- 826 50. M. Hargreaves, L. L. Spriet, Skeletal muscle energy metabolism during exercise. *Nat. Metab.* **2**, 817–828  
827 (2020).
- 828 51. W. Dudzinska, A. Lubkowska, B. Dolegowska, K. Safranow, Blood uridine concentration may be an  
829 indicator of the degradation of pyrimidine nucleotides during physical exercise with increasing intensity. *J.*  
830 *Physiol. Biochem.* **66**, 189–196 (2010).
- 831 52. H. A. Harper, Biochemistry of serotonin. *Dis. Colon Rectum* **7**, 83–86 (1964).
- 832 53. M. O. Melancon, D. Lorrain, I. J. Dionne, Exercise and sleep in aging: Emphasis on serotonin. *Pathol. Biol.*  
833 **62**, 276–283 (2014).
- 834 54. S. A. Romero, et al., Mast cell degranulation and de novo histamine formation contribute to sustained  
835 postexercise vasodilation in humans. *J. Appl. Physiol.* **122**, 603–610 (2017).
- 836 55. M. J. Luttrell, J. R. Halliwill, The Intriguing Role of Histamine in Exercise Responses. *Exerc. Sport Sci.*  
837 *Rev.* **45**, 16–23 (2017).
- 838 56. C. L. H. van Berlo, et al.,  $\gamma$ -Aminobutyric acid production in small and large intestine of normal and  
839 germfree Wistar rats Influence of food intake and intestinal flora. *Gastroenterology* **93**, 472–479 (1987).
- 840 57. L. G. Kirby, J. M. Chou-Green, K. Davis, I. Lucki, The effects of different stressors on extracellular  
841 5-hydroxytryptamine and 5-hydroxyindoleacetic acid. *Brain Res.* **760**, 218–230 (1997).
- 842 58. C. Stenfors, S. B. Ross, Changes in extracellular 5-HIAA concentrations as measured by in vivo  
843 microdialysis technique in relation to changes in 5-HT release. *Psychopharmacology* **172**, 119–128 (2004).
- 844 59. A. Kakee, et al., Efflux of a suppressive neurotransmitter, GABA, across the blood–brain barrier. *J.*  
845 *Neurochem.* **79**, 110–118 (2001).
- 846 60. J. R. Strawn, et al., Intra- and inter-individual relationships between central and peripheral serotonergic  
847 activity in humans: a serial cerebrospinal fluid sampling study. *Life Sci.* **71**, 1219–1225 (2002).
- 848 61. M. Gleeson, Interrelationship between Physical Activity and Branched-Chain Amino Acids 1. *J. Nutr.* **135**,  
849 1591S–1595S (2005).
- 850 62. G. Mann, S. Mora, G. Madu, O. A. J. Adegoke, Branched-chain Amino Acids: Catabolism in Skeletal  
851 Muscle and Implications for Muscle and Whole-body Metabolism. *Front. Physiol.* **12**, 702826 (2021).
- 852 63. P. Felig, The glucose-alanine cycle. *Metabolism* **22**, 179–207 (1973).
- 853 64. P. L. Greenhaff, The nutritional biochemistry of creatine. *J. Nutr. Biochem.* **8**, 610–618 (1997).
- 854 65. J. M. Hinkley, et al., Exercise and ageing impact the kynurenone/tryptophan pathway and acylcarnitine  
855 metabolite pools in skeletal muscle of older adults. *J. Physiol.* **601**, 2165–2188 (2023).
- 856 66. B. D. Paul, J. I. Sbodio, S. H. Snyder, Cysteine Metabolism in Neuronal Redox Homeostasis. *Trends*  
857 *Pharmacol. Sci.* **39**, 513–524 (2018).
- 858 67. M. Bandookwala, P. Sengupta, 3-Nitrotyrosine: a versatile oxidative stress biomarker for major  
859 neurodegenerative diseases. *Int. J. Neurosci.* **130**, 1047–1062 (2020).

- 860 68. G. Burnstock, Glioma Signaling. *Adv. Exp. Med. Biol.* **986**, 1–12 (2012).
- 861 69. S. Pathak, et al., The Influence of Kynurenine Metabolites on Neurodegenerative Pathologies. *Int. J. Mol. Sci.* **25**, 853 (2024).
- 862 70. J. B. Mistry, M. Bukhari, A. M. Taylor, Alkaptonuria. *Rare Dis.* **1**, e27475 (2014).
- 863 71. H. Huang, Y. Li, J. Liang, F. D. Finkelman, Molecular Regulation of Histamine Synthesis. *Front. Immunol.* **9**, 1392 (2018).
- 864 72. W. K. ALDERTON, C. E. COOPER, R. G. KNOWLES, Nitric oxide synthases: structure, function and inhibition. *Biochem. J.* **357**, 593 (2001).
- 865 73. A. A.-B. Badawy, Kynurenine Pathway of Tryptophan Metabolism: Regulatory and Functional Aspects. *Int. J. Tryptophan Res.* **10**, 1178646917691938 (2017).
- 866 74. A. Zeman, A. Zeman, P. Reading, The science of sleep. *Clin. Med.* **5**, 97–100 (2005).
- 867 75. M. M. Thakkar, Histamine in the regulation of wakefulness. *Sleep Med. Rev.* **15**, 65–74 (2011).
- 868 76. F. L. de Felipe, Revised Aspects into the Molecular Bases of Hydroxycinnamic Acid Metabolism in Lactobacilli. *Antioxidants* **12**, 1294 (2023).
- 869 77. E. J. Dennis, et al., Systems Neuroscience of Natural Behaviors in Rodents. *J. Neurosci.* **41**, 911–919 (2021).
- 870 78. P. Sterling, Allostasis: A model of predictive regulation. *Physiol. Behav.* **106**, 5–15 (2012).
- 871 79. S. Cinca-Morros, S. Garcia-Rey, J. Álvarez-Herms, L. Basabe-Desmonts, F. Benito-Lopez, A physiological perspective of the relevance of sweat biomarkers and their detection by wearable microfluidic technology: A review. *Anal. Chim. Acta* **1327**, 342988 (2024).
- 872 80. S. Teixido-Trujillo, et al., Measured GFR in murine animal models: review on methods, techniques, and procedures. *Pflügers Arch. - Eur. J. Physiol.* **475**, 1241–1250 (2023).
- 873 81. J. Liu, et al., Integrative analysis of the mouse fecal microbiome and metabolome reveal dynamic phenotypes in the development of colorectal cancer. *Front. Microbiol.* **13**, 1021325 (2022).
- 874 82. O. Deda, H. G. Gika, G. Theodoridis, Metabolic Profiling, Methods and Protocols. *Methods Mol. Biol.* **2891**, 153–163 (2025).
- 875 83. C. Touma, R. Palme, N. Sachser, Analyzing corticosterone metabolites in fecal samples of mice: a noninvasive technique to monitor stress hormones. *Horm. Behav.* **45**, 10–22 (2004).
- 876 84. C. Touma, N. Sachser, E. Möstl, R. Palme, Effects of sex and time of day on metabolism and excretion of corticosterone in urine and feces of mice. *Gen. Comp. Endocrinol.* **130**, 267–278 (2003).
- 877 85. J. R. St. Juliana, J. L. Bryant, N. Wielebnowski, B. P. Kotler, Physiological validation of a non-invasive method to evaluate adrenocortical activity and the time course for the excretion of stress hormones in the feces of three species of desert gerbils. *Isr. J. Ecol. Evol.* **65**, 21–27 (2019).
- 878 86. K. V. Thrivikraman, R. L. Huot, P. M. Plotsky, Jugular vein catheterization for repeated blood sampling in the unrestrained conscious rat. *Brain Res. Protoc.* **10**, 84–94 (2002).
- 879 87. T.-F. Yuan, L. (乐;娟 Juan, W. (王;少;亭 Shao-Ting, L. (李;艳 Yan, An LC/MS/MS method for analyzing the steroid metabolome with high accuracy and from small serum samples[S]. *J. Lipid Res.* **61**, 580–586 (2020).
- 880 88. R. Thakare, et al., Simultaneous LC–MS/MS analysis of eicosanoids and related metabolites in human serum, sputum and BALF. *Biomed. Chromatogr.* **32** (2018).
- 881 89. K. J. Bronsema, R. Bischoff, N. C. van de Merbel, High-Sensitivity LC-MS/MS Quantification of Peptides and Proteins in Complex Biological Samples: The Impact of Enzymatic Digestion and Internal Standard Selection on Method Performance. *Anal. Chem.* **85**, 9528–9535 (2013).
- 882 90. E. BLOMSTRAND, D. PERRETT, M. PARRY-BILLINGS, E. A. NEWSHOLME, Effect of sustained exercise on plasma amino acid concentrations and on 5-hydroxytryptamine metabolism in six different brain regions in the rat. *Acta Physiol. Scand.* **136**, 473–482 (1989).
- 883 91. V. Mante, D. Sussillo, K. V. Shenoy, W. T. Newsome, Context-dependent computation by recurrent dynamics in prefrontal cortex. *Nature* **503**, 78–84 (2013).

- 907 92. J. J. Davis, J. Thornham, M. G. Roper, Online LC-MS/MS Analysis for Profiling Peptide Hormone  
908 Secretion Dynamics from Islets of Langerhans. *Anal. Chem.* **97**, 4209–4216 (2025).
- 909 93. K. Sriyudthsak, F. Shiraishi, M. Y. Hirai, Mathematical Modeling and Dynamic Simulation of Metabolic  
910 Reaction Systems Using Metabolome Time Series Data. *Front. Mol. Biosci.* **3**, 15 (2016).
- 911 94. T. Huan, L. Li, Counting Missing Values in a Metabolite-Intensity Data Set for Measuring the Analytical  
912 Performance of a Metabolomics Platform. *Anal. Chem.* **87**, 1306–1313 (2015).
- 913 95. M. C. Cora, L. Kooistra, G. Travlos, Vaginal Cytology of the Laboratory Rat and Mouse. *Toxicol. Pathol.*  
914 **43**, 776–793 (2015).
- 915 96. D. Sen, R. A. Lazenby, Electrochemical Biosensor Arrays for Multiple Analyte Detection. *Anal. Sens.* **4**  
916 (2024).
- 917 97. M. Sharafeldin, J. F. Rusling, Multiplexed electrochemical assays for clinical applications. *Curr. Opin.*  
918 *Electrochem.* **39**, 101256 (2023).
- 919 98. C. M. Kho, S. K. E. A. Rahim, Z. A. Ahmad, N. S. Abdullah, A Review on Microdialysis Calibration  
920 Methods: the Theory and Current Related Efforts. *Mol. Neurobiol.* **54**, 3506–3527 (2017).
- 921 99. Y. D. Feunang, et al., ClassyFire: automated chemical classification with a comprehensive, computable  
922 taxonomy. *J. Cheminformatics* **8**, 61 (2016).